The stability of localized spikes for the 1-D Brusselator reaction–diffusion model

J. C. TZOU, Y. NEC and M. J WARD

Link to this article: http://journals.cambridge.org/abstract_S0956792513000089

How to cite this article:
J. C. TZOU, Y. NEC and M. J WARD The stability of localized spikes for the 1-D Brusselator
reaction–diffusion model. European Journal of Applied Mathematics, Available on CJO 2013
doi:10.1017/S0956792513000089

Request Permissions : Click here

The stability of localized spikes for the 1-D Brusselator reaction–diffusion model

J. C. TZOU[1], Y. NEC[2] and M. J. WARD[2]

[1]*Department of Engineering Sciences and Applied Mathematics, Northwestern University,
2145 Sheridan Road, Evanston, IL 60208-3125, USA*
email: `tzou.justin@gmail.com`
[2]*Department of Mathematics, University of British Columbia, Vancouver, British Columbia V6T 1Z2, Canada*
emails: `cranberryana@gmail.com`, `ward@math.ubc.ca`

In a one-dimensional domain, the stability of localized spike patterns is analysed for two closely related singularly perturbed reaction–diffusion (RD) systems with Brusselator kinetics. For the first system, where there is no influx of the inhibitor on the domain boundary, asymptotic analysis is used to derive a non-local eigenvalue problem (NLEP), whose spectrum determines the linear stability of a multi-spike steady-state solution. Similar to previous NLEP stability analyses of spike patterns for other RD systems, such as the Gierer–Meinhardt and Gray–Scott models, a multi-spike steady-state solution can become unstable to either a competition or an oscillatory instability depending on the parameter regime. An explicit result for the threshold value for the initiation of a competition instability, which triggers the annihilation of spikes in a multi-spike pattern, is derived. Alternatively, in the parameter regime when a Hopf bifurcation occurs, it is shown from a numerical study of the NLEP that an *asynchronous*, rather than synchronous, oscillatory instability of the spike amplitudes can be the dominant instability. The existence of robust asynchronous temporal oscillations of the spike amplitudes has not been predicted from NLEP stability studies of other RD systems. For the second system, where there is an influx of inhibitor from the domain boundaries, an NLEP stability analysis of a quasi-steady-state two-spike pattern reveals the possibility of dynamic bifurcations leading to either a competition or an oscillatory instability of the spike amplitudes depending on the parameter regime. It is shown that the novel *asynchronous* oscillatory instability mode can again be the dominant instability. For both Brusselator systems, the detailed stability results from NLEP theory are confirmed by rather extensive numerical computations of the full partial differential equations system.

Key words: Brusselator; Singular perturbations; Quasi-equilibria; Non-local eigenvalue problem; Hopf bifurcation; Asynchronous oscillatory instability; Dynamically triggered instability

1 Introduction

Spatially localized patterns arise from a wide variety of reaction–diffusion (RD) systems, with applications to chemical dynamics and biological modelling (cf. [29]), the spatial distribution of urban crime (cf. [14, 24]), electronic gas-discharge systems (cf. [23]) and many other areas. In particular, it is now well-known that localized spot patterns can exhibit a wide range of different instabilities, including spot oscillation, spot annihilation and spot

self-replication behaviour. Various topics related to the analysis of far-from-equilibrium patterns modelled by partial differential equation (PDE) systems are discussed in [19] and [11].

In this broad context, in this paper we study the stability of localized spike-type solutions to two closely related RD systems with Brusselator-type kinetics. The Brusselator system (see, e.g. [18, 20 or 28] and the references therein) is a well-known theoretical model for a simplified autocatalytic reaction. It describes the space–time dependence of the concentrations of the intermediate products U (the activator) and V (the inhibitor) in the sequence of reactions

$$E \to U, \quad B + U \to V + P, \quad 2U + V \to 3U, \quad U \to Q. \tag{1.1}$$
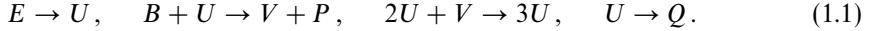
Assuming (without loss of generality) that all rate constants of the reactions in (1.1) are unity, the conventional dimensionless Brusselator model in a one-dimensional domain, with slow diffusion of the activator and constant influx of the inhibitor from the boundaries, can be written as

$$U_t = \epsilon_0^2 U_{xx} + \mathscr{E}_0 - (B_0 + 1)U + VU^2, \quad -1 < x < 1, \quad U_x(\pm 1, t) = 0, \quad t > 0, \tag{1.2a}$$
$$V_t = D_0 V_{xx} + B_0 U - VU^2, \quad -1 < x < 1, \quad V_x(\pm 1, t) = \pm \mathscr{A}_0, \quad t > 0, \tag{1.2b}$$

supplemented by appropriate initial conditions. Here $U \geqslant 0$, $V \geqslant 0$, $0 < \epsilon_0 \ll 1$, and $\mathscr{A}_0$, B_0, D_0 and $\mathscr{E}_0$ are all non-negative constants. The constant $\mathscr{A}_0$ represents a boundary feed term for the inhibitor, while the constant $\mathscr{E}_0$ represents a constant bulk feed for the activator. Our key assumption in the model is that there is an asymptotically large ratio of the diffusivities for U and V.

In the absence of a boundary feed-term so that $\mathscr{A}_0 = 0$ in (1.2b), spikes for (1.2) occur when $\mathscr{E}_0 = \mathcal{O}(\epsilon_0^{1/2})$ (see Appendix and [27]). Upon writing $\mathscr{E}_0 = \epsilon_0^{1/2} E_0$, where $E_0 = \mathcal{O}(1)$, the scaling analysis in Appendix yields

$$u_t = \epsilon^2 u_{xx} + \epsilon - u + fvu^2, \quad -1 < x < 1, \quad u_x(\pm 1, t) = 0, \quad t > 0, \tag{1.3a}$$

$$\tau v_t = D v_{xx} + \frac{1}{\epsilon}\left(u - vu^2\right), \quad -1 < x < 1, \quad v_x(\pm 1, t) = 0, \quad t > 0, \tag{1.3b}$$

where t is a different time-scale than in (1.2). Here D, τ, ϵ and f are defined by

$$D \equiv \frac{D_0(B_0 + 1)^{3/2}}{E_0^2}, \quad \tau \equiv \frac{(B_0 + 1)^{5/2}}{E_0^2}, \quad \epsilon \equiv \frac{\epsilon_0}{\sqrt{B_0 + 1}}, \quad f \equiv \frac{B_0}{B_0 + 1}. \tag{1.4}$$

In contrast, when both the boundary and bulk feed terms are non-vanishing, and are asymptotically small of the order $\mathcal{O}(\epsilon_0^{1/2})$ so that $\mathscr{E}_0 = \epsilon_0^{1/2} E_0$ and $\mathscr{A}_0 = \epsilon_0^{1/2} A_0$, where E_0 and A_0 are $\mathcal{O}(1)$, then the appropriate re-scaled form of (1.2) is (see Appendix)

$$u_t = \epsilon^2 u_{xx} + \epsilon E - u + fvu^2, \quad -1 < x < 1, \quad u_x(\pm 1, t) = 0, \quad t > 0, \tag{1.5a}$$

$$\tau v_t = D v_{xx} + \frac{1}{\epsilon}\left(u - vu^2\right), \quad -1 < x < 1, \quad v_x(\pm 1, t) = \pm 1, \quad t > 0. \tag{1.5b}$$

where D, E, τ, ϵ and f are now defined as

$$D \equiv \frac{D_0 A_0^2 \sqrt{B_0 + 1}}{B_0^2}, \quad E \equiv \frac{E_0 A_0}{B_0 \sqrt{B_0 + 1}}, \quad \tau \equiv \frac{A_0^2 (B_0 + 1)^{3/2}}{B_0^2}, \quad \epsilon \equiv \frac{\epsilon_0}{\sqrt{B_0 + 1}},$$

$$f \equiv \frac{B_0}{B_0 + 1}. \tag{1.6}$$

The spatially uniform steady-state solution of (1.3) is $u_e = \epsilon/(1 - f)$ and $v_e = \epsilon^{-1}(1-f)$. For arbitrary $\epsilon > 0$, it is well known that this solution undergoes either a Turing or Hopf instability depending on the parameter ranges in (1.3) (cf. [18]). Near the bifurcation points for the onset of these instabilities, small-amplitude patterns emerge and they have been well studied in a multi-spatial dimensional context through canonical amplitude equations that are readily derived from a multi-scale weakly nonlinear analysis (see [20] and the references therein). For a detailed survey of normal form theory as applied to the study of one-dimensional pattern formation in the Brusselator model see [36]. More recently, a weakly nonlinear analysis was used in [26] to study pattern formation near the Turing–Hopf bifurcation in a Brusselator model with superdiffusion.

In contrast, with an asymptotically large diffusivity ratio as in (1.3), localized large-amplitude patterns are readily observed in full numerical simulations of (1.3) with initial conditions close to the spatially uniform state (u_e, v_e). A standard calculation shows that for $f > 1/2$, $0 < \epsilon \ll 1$ and $\tau = o(1)$, the band of unstable wave numbers m for an instability mode of the form $(u, v) = (u_e, v_e) + e^{\lambda t + imx}(\Phi, N)$ satisfies

$$\epsilon^{1/2} \left[(2f - 1)(1 - f)D\right]^{-1/2} < m < \frac{(2f - 1)^{1/2}}{\epsilon}, \qquad \text{as} \quad \epsilon \to 0. \tag{1.7}$$

The maximum growth rate within this instability band is calculated as $\lambda_{\max} \sim (2f - 1) - 2\epsilon^2 m^2$, which occurs when $m = m_{\max}$, where

$$m_{\max} \sim \left(\frac{f}{D(f - 1)^2}\right)^{1/4} \epsilon^{-1/4}, \qquad \text{as} \quad \epsilon \to 0. \tag{1.8}$$

Therefore, the instability has a short wavelength of $\mathcal{O}(\epsilon^{1/4})$. In contrast, our results (see (1.9) and (1.10)) show that stable localized spikes occur only at $\mathcal{O}(1)$ inter-spike separation distances. This suggests that starting from initial data a coarsening process must occur, which eventually leads to localized spikes. For a particular parameter set, in Figure 1 we show the formation of a two-spike pattern as obtained from the numerical solution of (1.3).

Rigorous results for the existence of large amplitude equilibrium solutions for some generalizations of the Brusselator model (1.3) in the non-singular perturbation limit $\epsilon = 1$ have recently been obtained in [21] and [22] (see also the references therein). However, to date, there is no comprehensive stability theory for these large amplitude solutions.

In a more general one-dimensional context, there are now many results for the existence and stability of localized equilibrium spike patterns for various singularly perturbed two-component RD systems such as the Gierer–Meinhardt (GM) model [5, 9, 32, 34], the Gray–Scott (GS) model [1, 4, 12, 16, 17] and the Schnakenberg model [10, 31]. An explicit characterization of the slow dynamics of spike patterns, and their instability mechanisms,
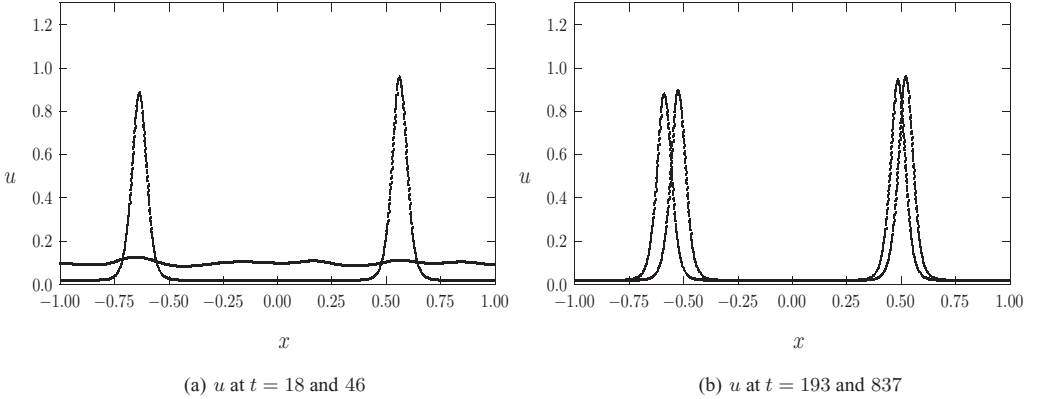
(a) u at $t = 18$ and 46

(b) u at $t = 193$ and 837

FIGURE 1. Plot of numerical solution u of (1.3) at different times for the parameter set $\epsilon = 0.02$, $f = 0.8$, $D = 0.1$ and $\tau = 0.001$, with initial condition $u(x, 0) = u_e(1 + 0.02 \times \text{rand})$ and $v(x, 0) = v_e(1 + 0.02 \times \text{rand})$, where $u_e = \epsilon/(1 - f)$, $v_e = \epsilon^{-1}(1 - f)$ and rand is a uniformly generated random number in $[0, 1]$. Left: the small amplitude pattern at $t = 18$ leads to the two-spike pattern shown at $t = 46$. Right: As t increases from $t = 193$ to 837, the two spikes slowly drift to their equilibrium locations at $x = \pm 0.5$.

is given in [2, 3, 6–8, 25] for various RD systems in one dimension. A central feature in all of these previous studies is that the determination of the spectrum of various classes of non-local eigenvalue problems (NLEPs) is critical for characterizing the stability of both equilibrium and quasi-equilibrium multi-spike patterns. A survey of the NLEP theory is given in [35].

The goal of this paper is to provide a detailed analysis of the stability of multi-spike equilibria of (1.3), and a detailed study of the dynamics and stability of two-spike solutions for the Brusselator model (1.5) with a non-zero boundary feed term. Although much of the general theoretical framework for the spike-stability analysis is closely related to that developed in previous works for GM, GS and Schnakenberg RD systems, there are important differences both in the details of the analysis required and in the stability results that are obtained. The stability results obtained herein complement the results obtained in the companion paper [27] for the dynamics of spikes in the Brusselator model.

We now summarize our main results. In Section 2.1 we begin by briefly outlining the asymptotic construction of symmetric N-spike equilibrium solutions to (1.3). We refer to a symmetric N-spike solution as one for which the spikes are equally spaced and, correspondingly, each spike has the same amplitude. The main focus of Section 2, not considered in [27], is to analyse the stability of symmetric N-spike equilibrium solutions to (1.3). A singular perturbation analysis is used in Section 2.2 to derive an NLEP that determines the stability of this solution to $\mathcal{O}(1)$ time-scale instabilities. The derivation of this NLEP is rather more intricate than for related RD systems in [4, 5, 9, 10, 12, 17, 31, 32] owing primarily to the presence of two separate non-local terms resulting from the $\mathcal{O}(\epsilon^{-1})$ coefficient in (1.3b), and secondarily from the non-trivial background state for the activator resulting from the constant feed term of order $\mathcal{O}(\epsilon)$ in (1.3a). From an analysis of this NLEP there are two distinct mechanisms through which the solution can go unstable as the bifurcation parameters τ and D are varied.

Firstly, for τ sufficiently small, our analysis of the NLEP in Section 2.3 reveals the existence of a critical threshold N_{c+} such that a pattern consisting of N spikes with $N > 1$ is unstable to a competition instability if and only if $N > N_{c+}$. This instability, which develops on an $\mathcal{O}(1)$ time-scale as $\epsilon \to 0$, is due to a positive real eigenvalue, and it triggers the collapse of some of the spikes in the overall pattern. This critical threshold $N_{c+} > 0$ is the unique root of (see Principal Results 2.3 and 2.4)

$$N \left(1 + \cos\left(\pi/N\right)\right)^{1/3} = \left(\frac{2f^2}{3(1-f)D}\right)^{1/3} . \tag{1.9}$$

In addition, from the location of the bifurcation point associated with the birth of an asymmetric N-spike equilibrium solution, a further threshold N_{c-} is derived that predicts that an N-spike equilibrium solution with $N > 1$ is stable with respect to slow translational instabilities of the spike locations if and only if $N < N_{c-}$, where (see (2.47))

$$N_{c-} = \left(\frac{2f^2}{3(1-f)D}\right)^{1/3} . \tag{1.10}$$

Since $N_{c-} < N_{c+}$, the stability properties of an N-spike equilibrium solution to (1.3) with $N > 1$ and τ sufficiently small are as follows: stability when $N < N_{c-}$; stability with respect to fast $\mathcal{O}(1)$ time-scale instabilities but unstable with respect to slow translation instabilities when $N_{c-} < N < N_{c+}$; a fast $\mathcal{O}(1)$ time-scale instability dominates when $N > N_{c+}$. We remark that for (1.3) posed on a domain of length L, by a scaling argument we need only replace D in (1.9) and (1.10) with $4D/L^2$. As an example, consider the parameter set $\epsilon = 0.02$, $f = 0.8$ and $\tau = 0.001 \ll 1$. Then the threshold (1.10) with $N_{c-} = 2$ predicts that a two-spike pattern is stable to both fast and slow instabilities when $D < 0.133$. The numerical results shown in Figure 1 with $D = 0.1$ confirm this prediction.

For the case $\tau > 0$ in (1.3), we show that an N-spike equilibrium solution to (1.3) is unstable when $N > N_{c+}$, or equivalently when $D > D_{c_N}$ (see Principal Result 2.3), where

$$D_{c_N} \equiv \frac{2f^2}{3N^3(1-f)\left(1 + \cos\frac{\pi}{N}\right)} .$$

For $D < D_{c_N}$, in Section 2.4 we show from a numerical computation of the spectrum of the NLEP that there is a critical value τ_H of τ for which an N-spike equilibrium solution undergoes a Hopf bifurcation. In contrast to the previous NLEP stability studies of [12, 30, 32] for the GM and GS models, where a synchronous oscillation in the spike amplitudes was always the dominant instability, our results show that there is a parameter regime where the Hopf bifurcation for the Brusselator (1.3) triggers robust *asynchronous* temporal oscillations of spike amplitudes. Furthermore, we establish the scaling law $\tau_H \sim c/D$ as $D \to 0$ for some $\mathcal{O}(1)$ constant $c > 0$. Therefore, in contrast to the previous analyses for the GM and GS models (cf. [12, 32]) where $\tau_H = \mathcal{O}(1)$ as $D \to 0$, this new scaling law indicates that spikes that are isolated from their neighbours or from the domain boundaries (i.e. D small) do not undergo an oscillatory instability unless τ is very large.

For the boundary-flux system (1.5), in Section 3.1 we derive an Ordinary Differential Equation (ODE) for the slow evolution of a two-spike quasi-steady pattern. In the presence of boundary flux, equilibrium spikes are not equally spaced, and depending on the parameter values, slowly drifting spikes may annihilate against the domain boundaries. In Section 3.2 we derive an NLEP governing the stability of the two-spike quasi-steady pattern to $\mathcal{O}(1)$ time-scale instabilities. From an analytical and numerical study of this NLEP, in Sections 3.3 and 3.4 we show the possibility of dynamic bifurcations leading to either a competition or an oscillatory instability of spike amplitudes depending on the parameter regime. As in the study of the no-flux system (1.3), the novel *asynchronous* oscillatory instability mode can again be the dominant instability.

For both Brusselator systems, the detailed stability results are confirmed and illustrated by rather extensive numerical computations of the full PDE systems.

2 Stability of symmetric N-spike equilibria with no boundary flux

In this section, we construct N-spike symmetric equilibrium solutions of (1.3). By a symmetric spike solution we refer to a pattern of spikes with a common height and equal spacing. We then linearize about this equilibrium solution to derive an NLEP governing the stability of the equilibrium pattern to $\mathcal{O}(1)$ eigenvalues. Stability with respect to the small $\mathcal{O}(\epsilon^2)$ eigenvalues as well as the existence of asymmetric equilibria were studied in [27]. We highlight the differences between the NLEP derived here and analogous NLEPs derived for the GS ([12]) and GM ([32]) models. We also draw similarities to the aforementioned NLEPs and appeal to results of [32] to determine criteria for competition and oscillatory instabilities. Numerical results computed from (1.3) are used to validate our stability results.

2.1 Asymptotic construction of N-spike equilibria

To construct an N-spike symmetric equilibrium solution, characterized by spikes of a common amplitude and equal spacing, we employ the 'gluing' technique used in [31]. We first consider a one-spike solution on the interval $|x| < \ell$ centred at $x = 0$. In the inner region of width $\mathcal{O}(\epsilon)$, we introduce the stretched spatial variable $y = \epsilon^{-1}x$ and let $U(y) = u(\epsilon y)$. Because v varies on an $\mathcal{O}(1)$ length scale, $v \sim v_c$ in the inner region where the constant v_c is to be found. Then, by (1.3a), we obtain to leading order that U satisfies $U_{yy} - U + fv_cU^2 = 0$. The spike solution to this problem is

$$U(y) = \frac{1}{fv_c}w(y), \tag{2.1}$$

where $w = \frac{3}{2}\operatorname{sech}^2(y/2)$ is the homoclinic solution to

$$w'' - w + w^2 = 0, \quad -\infty < y < \infty, \quad w \to 0 \text{ as } |y| \to \infty, \quad w'(0) = 0, \quad w(0) > 0, \tag{2.2}$$

for which

$$\int_{-\infty}^{\infty} w \, dy = \int_{-\infty}^{\infty} w^2 \, dy = 6. \tag{2.3}$$

In the outer region, we obtain from (1.3a) that $u = \mathcal{O}(\epsilon)$ so that $vu^2 \ll u$. Thus, $u \sim \epsilon$ to leading order in the outer region. The resulting leading-order composite solution for u is then given by

$$u \sim \epsilon + \frac{1}{fv_c} w(x/\epsilon), \tag{2.4}$$

where $w(y)$ is defined by (2.2). Since u is localized near $x = 0$, the terms involving u in (1.3b) can be represented in the outer region as delta functions. Upon using (2.3) and (2.4) we calculate that

$$\frac{1}{\epsilon}(u - vu^2) \sim 1 + \left(\frac{1}{fv_c}\int_{-\infty}^{\infty} w\, dy - \frac{1}{f^2 v_c}\int_{-\infty}^{\infty} w^2\, dy\right)\delta(x) = 1 + \frac{6}{fv_c}\left(1 - \frac{1}{f}\right)\delta(x). \tag{2.5}$$

Therefore, in the outer region we obtain for $\epsilon \to 0$ that v satisfies

$$Dv_{xx} + 1 = \frac{6}{fv_c}\left(\frac{1}{f} - 1\right)\delta(x), \quad -\ell < x < \ell, \quad v_x(\pm\ell) = 0. \tag{2.6}$$

Integrating this equation over $|x| \leqslant \ell$ and imposing that $v_x = 0$ at $x = \pm\ell$, we obtain

$$v_c = \frac{3}{f\ell}\left(\frac{1}{f} - 1\right) > 0, \tag{2.7}$$

since f satisfies $0 < f < 1$. To obtain an N-spike equilibrium solution for (1.3) on the domain of length two, we must set $2 = 2N\ell$ and periodically extend our solution on $|x| < l$ to $[-1, 1]$. Thus, we identify that $l = 1/N$ and (2.7) becomes

$$v_c = \frac{3N}{f}\left(\frac{1}{f} - 1\right). \tag{2.8}$$

Before solving for the outer solution for v, we make some remarks. Firstly, v_c in (2.8) increases with N, and so, by (2.1), the common spike amplitude decreases as the number of spikes increases. Also, the common amplitude is independent of D, which will not be the case when we construct spike solutions in the presence of boundary flux in Section 3. Secondly, by using $\ell = 1/N$, the centre of each spike is located at

$$x_j = -1 + \frac{2j + 1}{N}, \quad j = 0, \ldots, N - 1. \tag{2.9}$$

This equally spaced spike result will be shown not to hold in Section 3 when we allow for the presence of boundary flux. Lastly, the uniqueness of the solution to (2.6) is achieved by imposing the matching condition $v(x_j) = v_c$.

Using the last remark, we write the equation for v on the interval $-1 < x < 1$ as

$$Dv_{xx} + 1 = \frac{6}{fv_c}\left(\frac{1}{f} - 1\right)\sum_{j=0}^{N-1}\delta(x - x_j), \quad -1 < x < 1, \quad v_x(\pm 1) = 0, \tag{2.10}$$

where v_c satisfies (2.8). The solution to (2.10) can be written in terms of the Neumann

Green's function $G(x; x_j)$ as

$$v = \bar{v} + \frac{6}{f v_c} \left(\frac{1}{f} - 1 \right) \sum_{j=0}^{N-1} G(x; x_j) \tag{2.11}$$

for some constant $\bar{v}$ to be determined. Here $G(x; x_j)$ satisfies

$$D G_{xx}(x; x_j) + \frac{1}{2} = \delta(x - x_j), \quad -1 < x < 1; \quad G_x(\pm 1; x_j) = 0, \quad \int_{-1}^{1} G(x; x_j)\, dx = 0, \tag{2.12}$$

which has the explicit solution

$$G(x; x_j) = -\frac{1}{4D}(x^2 + x_j^2) + \frac{1}{2D}|x - x_j| - \frac{1}{6D}. \tag{2.13}$$

The constant $\bar{v}$ is determined by the matching condition $v(x_i) = v_c$, yielding

$$\bar{v} = v_c - \frac{6}{f v_c} \left(\frac{1}{f} - 1 \right) \sum_{j=0}^{N-1} G(x_i; x_j), \tag{2.14}$$

where the right-hand side of (2.14) is readily shown to be independent of i. We summarize our result as follows.

Principal Result 2.1 *Let $\epsilon \to 0$ in (1.3). Then the leading-order composite approximation for the symmetric N-spike equilibrium solution for u is*

$$u_e(x) \sim \epsilon + \frac{1}{f v_c} \sum_{j=0}^{N-1} w[\epsilon^{-1}(x - x_j)]. \tag{2.15a}$$

Alternatively, the outer solution for v valid for $|x - x_j| \gg \mathcal{O}(\epsilon)$ and $j = 0, \ldots, N-1$ is given asymptotically by

$$v_e(x) \sim \bar{v} + \frac{6}{f v_c} \left(\frac{1}{f} - 1 \right) \sum_{j=0}^{N-1} G(x; x_j). \tag{2.15b}$$

Here $w(y)$ satisfies (2.2), while v_c, x_j, $\bar{v}$ and $G(x; x_j)$ are given in (2.8), (2.9), (2.14) and (2.13), respectively.

Next, we calculate the critical value D_{S_N} of D for which an asymmetric N-spike equilibrium solution, characterized by spikes of different heights and non-uniform spacing, bifurcates from the symmetric N-spike symmetric solution branch. This bifurcation point corresponds to a zero eigenvalue crossing along the symmetric branch, and for τ sufficiently small, it characterizes the stability threshold of symmetric N-spike equilibria with respect to the small eigenvalues with $\lambda \to 0$ as $\epsilon \to 0$ in the linearization of (1.3) (cf. [27]).

To determine this bifurcation point, we compute $v(l)$ for the one-spike equilibrium solution to (1.3) on the domain $-l < x < l$. From (2.6) and (2.7), we readily calculate that

$$v(l) = \frac{1}{2D}\left(l^2 + \frac{b}{l}\right), \qquad b \equiv \frac{6D}{f^2}(1-f).$$

The bifurcation point for the emergence of an asymmetric N-spike solution on a domain of length two is obtained by calculating the minimum point of the graph of $v(l)$ versus l, and then setting $2Nl = 2$ (cf. [27]). This occurs at the value $D = D_{s_N}$, where

$$D_{s_N} \equiv \frac{f^2}{3(1-f)N^3}. \tag{2.16}$$

2.2 Derivation of non-local eigenvalue problem

To analyse the stability of the equilibrium solution constructed above, we linearize about u_e and v_e, where u_e and v_e are given in (2.15a) and (2.15b), respectively. We substitute $u = u_e + e^{\lambda t}\Phi$ and $v = v_e + e^{\lambda t}\Psi$ into (1.3), where $|\Phi| \ll 1$ and $|\Psi| \ll 1$. This leads to the eigenvalue problem

$$\epsilon^2 \Phi_{xx} - \Phi + 2fu_e v_e \Phi + fu_e^2 \Psi = \lambda \Phi, \quad -1 < x < 1, \quad \Phi_x(\pm 1) = 0, \tag{2.17a}$$

$$D\Psi_{xx} + \frac{1}{\epsilon}\left[\Phi - 2u_e v_e \Phi - u_e^2 \Psi\right] = \tau\lambda\Psi, \quad -1 < x < 1, \quad \Psi_x(\pm 1) = 0. \tag{2.17b}$$

To analyse the large eigenvalues that are $\mathcal{O}(1)$ as $\epsilon \to 0$, we look for a localized eigenfunction for Φ of the form

$$\Phi \sim \sum_{j=0}^{N-1} \Phi_j[\epsilon^{-1}(x - x_j)], \tag{2.18}$$

with $\Phi_j \to 0$ exponentially as $|y| \to \infty$. In the inner region near the jth spike we obtain from (2.17b) that $\Psi \sim \Psi_j$, where Ψ_j is a constant to be found. Since both u_e and Φ are localized near each x_j, we calculate in the sense of distributions that

$$\frac{1}{\epsilon}\left[\Phi - 2u_e v_e \Phi - u_e^2 \Psi\right] \sim \left(\int_{-\infty}^{\infty}\Phi_j\,dy - \frac{2}{f}\int_{-\infty}^{\infty}w\Phi_j\,dy - \frac{\Psi_j}{f^2 v_c^2}\int_{-\infty}^{\infty}w^2\,dy\right)\delta(x - x_j). \tag{2.19}$$

Substituting (2.18) into (2.17a) and (2.19) into (2.17b), and using (2.3) for the last integral in (2.19), we obtain that

$$\Phi_j'' - \Phi_j + 2w\Phi_j + \frac{1}{fv_c^2}w^2\Psi_j = \lambda\Phi_j, \quad -\infty < y < \infty, \quad \Phi_j \to 0 \text{ as } |y| \to \infty, \tag{2.20a}$$

and

$$\Psi_{xx} - \mu^2\Psi = -\sum_{j=0}^{N-1}\tilde{\omega}_j\delta(x - x_j), \quad -1 < x < 1, \quad \Psi_x(\pm 1) = 0, \tag{2.20b}$$

where we have defined μ and $\tilde{\omega}_j$ by

$$\mu \equiv \sqrt{\frac{\tau\lambda}{D}}, \quad \tilde{\omega}_j \equiv \frac{1}{D}\left[\int_{-\infty}^{\infty}\Phi_j\,dy - \frac{2}{f}\int_{-\infty}^{\infty}w\Phi_j\,dy - \frac{6\Psi_j}{f^2v_c^2}\right]. \tag{2.21}$$

To derive an NLEP for Φ_j, we must compute Ψ_j for $j = 0,\dots,N-1$ from (2.20b). To do so, we write $\Psi(x)$ as

$$\Psi = \sum_{j=0}^{N-1} G^{(\mu)}(x;x_j)\tilde{\omega}_j, \tag{2.22}$$

where $G^{(\mu)}(x;x_j)$ is the Neumann Green's function satisfying

$$G_{xx}^{(\mu)} - \mu^2 G^{(\mu)} = -\delta(x - x_j), \quad -1 < x < 1\,; \quad G_x^{(\mu)}(\pm 1;x_j) = 0. \tag{2.23}$$

Evaluating (2.22) at $x = x_i$, we obtain that $\Psi(x_i) = \Psi_i = \sum_{j=0}^{N-1} G_{i,j}^{(\mu)}\tilde{\omega}_j$, where $G_{i,j}^{(\mu)} \equiv G^{(\mu)}(x_i,x_j)$ and $\tilde{\omega}_j$ is given in (2.21). In matrix form, this system can be written as

$$\boldsymbol{\Psi} = \mathscr{G}^{(\mu)}\left(\boldsymbol{\omega} - \frac{6}{f^2v_c^2D}\boldsymbol{\Psi}\right), \tag{2.24}$$

where

$$\boldsymbol{\Psi} \equiv \begin{pmatrix} \Psi_0 \\ \vdots \\ \Psi_{N-1} \end{pmatrix}, \quad \mathscr{G}^{(\mu)} \equiv \begin{pmatrix} G_{0,0}^{(\mu)} & G_{0,1}^{(\mu)} & \cdots & G_{0,N-1}^{(\mu)} \\ G_{1,0}^{(\mu)} & \ddots & \cdots & G_{1,N-1}^{(\mu)} \\ \vdots & \vdots & \ddots & \vdots \\ G_{N-1,0}^{(\mu)} & G_{N-1,1}^{(\mu)} & \cdots & G_{N-1,N-1}^{(\mu)} \end{pmatrix}, \tag{2.25}$$

and

$$\boldsymbol{\omega} = \frac{1}{D}\left[\int_{-\infty}^{\infty}\boldsymbol{\Phi}\,dy - \frac{2}{f}\int_{-\infty}^{\infty}w\boldsymbol{\Phi}\,dy\right], \quad \boldsymbol{\Phi} \equiv \begin{pmatrix} \Phi_0 \\ \vdots \\ \Phi_{N-1} \end{pmatrix}. \tag{2.26}$$

Solving for $\boldsymbol{\Psi}$ in (2.24), we obtain

$$\boldsymbol{\Psi} = \mathscr{C}^{-1}\mathscr{G}^{(\mu)}\boldsymbol{\omega}\,; \quad \mathscr{C} \equiv \mathscr{I} + \frac{6}{f^2v_c^2D}\mathscr{G}^{(\mu)}, \tag{2.27}$$

where $\mathscr{I}$ is the $N \times N$ identity matrix.

Having obtained $\boldsymbol{\Psi}$ in terms of $\boldsymbol{\Phi}$, we now derive a vector NLEP for $\boldsymbol{\Phi}$. Upon defining the local operator L_0 by

$$L_0\phi \equiv \phi'' - \phi + 2w\phi, \tag{2.28}$$

we then use (2.26) for $\boldsymbol{\omega}$ to write (2.20a) in vector form as

$$L_0\boldsymbol{\Phi} + \frac{w^2}{fv_c^2D}\mathscr{C}^{-1}\mathscr{G}^{(\mu)}\left[\int_{-\infty}^{\infty}\left(\boldsymbol{\Phi} - \frac{2}{f}w\boldsymbol{\Phi}\right)dy\right] = \lambda\boldsymbol{\Phi}. \tag{2.29}$$

To obtain N uncoupled scalar NLEPs, we diagonalize $\mathscr{C}^{-1}$ and $\mathscr{G}^{(\mu)}$ by using the eigenpairs $\mathscr{G}^{(\mu)} v_j = \kappa_j v_j$ for $j = 0, \ldots, N-1$ of $\mathscr{G}^{(\mu)}$. This yields

$$\mathscr{G}^{(\mu)} = \mathscr{S} \Lambda \mathscr{S}^{-1}, \quad \mathscr{C}^{-1} = \mathscr{S} \left[\mathscr{I} + \beta_0 \Lambda \right]^{-1} \mathscr{S}^{-1}; \quad \beta_0 \equiv \frac{6}{f^2 v_c^2 D}, \tag{2.30}$$

where $\mathscr{S}$ is the non-singular matrix whose columns are the eigenvectors of $\mathscr{G}^{(\mu)}$ and Λ is the diagonal matrix of the eigenvalues $\kappa_0, \ldots, \kappa_{N-1}$. From the observation that $\left(\mathscr{G}^{(\mu)} \right)^{-1}$ is a tri-diagonal matrix, explicit formulae for these eigenvalues were calculated in Proposition 2 of [9] as

$$\kappa_j = \frac{1}{\mu \sigma_j}, \quad j = 0, \ldots, N-1, \tag{2.31}$$

where σ_j for $j = 0, \ldots, N-1$ are given by

$$\sigma_0 = e_\lambda + 2 f_\lambda; \quad \sigma_j = e_\lambda + 2 f_\lambda \cos \left(\frac{j\pi}{N} \right), \quad j = 1, \ldots, N-1. \tag{2.32a}$$

Here e_λ and f_λ are defined in terms of $\mu \equiv \sqrt{\tau \lambda / D}$ by

$$e_\lambda \equiv 2 \coth \left(\frac{2\mu}{N} \right), \quad f_\lambda \equiv -\operatorname{csch} \left(\frac{2\mu}{N} \right). \tag{2.32b}$$

The corresponding eigenvectors of $\mathscr{G}^{(\mu)}$ are

$$v_0^t = (1, \ldots, 1); \quad v_{\ell,j} = \cos \left[\frac{j\pi}{N} (\ell - 1/2) \right], \quad j = 1, \ldots, N-1, \tag{2.32c}$$

where t denotes the transpose and $v_{\ell,j}$ denotes the ℓth component of the vector v_j.

Upon substituting (2.30) into (2.29), and making use of the transformation $\boldsymbol{\Phi} = \mathscr{S} \hat{\boldsymbol{\Phi}}$, we obtain the diagonal NLEP

$$L_0 \hat{\boldsymbol{\Phi}} + f \beta_0 \left[\mathscr{I} + \beta_0 \Lambda \right]^{-1} \Lambda w^2 \left(\frac{\int_{-\infty}^{\infty} \left(\hat{\boldsymbol{\Phi}} - \frac{2}{f} w \hat{\boldsymbol{\Phi}} \right) dy}{\int_{-\infty}^{\infty} w^2 \, dy} \right) = \lambda \hat{\boldsymbol{\Phi}}, \tag{2.33}$$

where β_0 is defined in (2.30), and where we have used $\int_{-\infty}^{\infty} w^2 \, dy = 6$. While the components of $\hat{\boldsymbol{\Phi}}$ are generally different, for notational convenience we label $\hat{\boldsymbol{\Phi}} = \hat{\Phi} e$, where e is the N-vector $(1, \ldots, 1)^t$. Since Λ is the diagonal matrix of eigenvalues κ_j, this substitution leads to N uncoupled scalar NLEPs of the form

$$L_0 \hat{\Phi} + f \tilde{\chi}_j w^2 \left(\frac{\int_{-\infty}^{\infty} \left(\hat{\Phi} - \frac{2}{f} w \hat{\Phi} \right) dy}{\int_{-\infty}^{\infty} w^2 \, dy} \right) = \lambda \hat{\Phi}, \quad j = 0, \ldots, N-1, \tag{2.34}$$

where $\tilde{\chi}_j$ is defined by

$$\tilde{\chi}_j \equiv \frac{\beta_0 \kappa_j}{1 + \beta_0 \kappa_j}. \tag{2.35}$$

In contrast to the NLEP problems for the GM and GS models analysed in [32] and [12], the NLEP (2.34) involves the two separate non-local terms $\int_{\infty}^{\infty} \hat{\Phi} \, dy$ and $\int_{\infty}^{\infty} w \hat{\Phi} \, dy$. These terms arise from the fact that the $\mathcal{O}(\epsilon^{-1})$ term in (1.3b) involves the sum of two localized terms. Due to this complication, it initially appears that the general theory developed in [32] is not applicable. However, as we now show, by a simple manipulation we can recast (2.34) into the same general form as the NLEP analysed in [32].

To do so, we first define I_1 and I_2 as $I_1 \equiv \int_{-\infty}^{\infty} \hat{\Phi} \, dy$ and $I_2 \equiv \int_{-\infty}^{\infty} w \hat{\Phi} \, dy$. Then by using (2.28) for $L_0 \hat{\Phi}$, together with the condition that $\hat{\Phi} \to 0$ as $|y| \to \infty$, we integrate (2.34) over $-\infty < y < \infty$ to obtain

$$-I_1 + 2I_2 + f \tilde{\chi}_j \left[I_1 - \frac{2}{f} I_2 \right] = \lambda I_1 \, , \tag{2.36}$$

which is then rearranged to yield

$$I_1 - \frac{2}{f} I_2 = -\frac{2}{f} \left[\frac{1 + \lambda - f}{1 + \lambda - \tilde{\chi}_j f} \right] I_2 \, . \tag{2.37}$$

Finally, using (2.37) in (2.34), we obtain the NLEP problem

$$L_0 \hat{\Phi} - \chi_j w^2 \left(\frac{\int_{-\infty}^{\infty} w \hat{\Phi} \, dy}{\int_{-\infty}^{\infty} w^2 \, dy} \right) = \lambda \hat{\Phi} \, , \quad \chi_j \equiv 2 \tilde{\chi}_j \left[\frac{1 + \lambda - f}{1 + \lambda - \tilde{\chi}_j f} \right] \, , \tag{2.38}$$

where $\tilde{\chi}_j$ is defined in terms of κ_j in (2.35).

The NLEP in (2.38) is of the form given in Proposition 3.3 of [32] for the GM model and in Principal Result 3.2 of [12] for the GS model. However, because the activator in the Brusselator model acts as two separate sources for the inhibitor, the identity (2.37) is needed, which results in a rather complicated coefficient in front of the non-local term in (2.38). Finally, by substituting (2.35) and (2.31) into (2.38) we obtain the following main result:

Principal Result 2.2 *Let $\epsilon \to 0$ in (1.3) and consider the N-spike equilibrium solution constructed in Section 2.1. The stability of this solution on an $\mathcal{O}(1)$ time-scale is determined by the spectrum of the NLEP*

$$L_0 \hat{\Phi} - \chi_j w^2 \left(\frac{\int_{-\infty}^{\infty} w \hat{\Phi} \, dy}{\int_{-\infty}^{\infty} w^2 \, dy} \right) = \lambda \hat{\Phi} \, , \quad -\infty < y < \infty \, , \quad \hat{\Phi} \to 0 \ \ as \ \ |y| \to \infty \, , \tag{2.39a}$$

where χ_j is given explicitly by

$$\chi_j = \frac{2}{1 + \mu \sigma_j / \beta_0} \left[1 + \frac{f \mu \sigma_j}{f \beta_0 - (1 + \lambda)(\beta_0 + \mu \sigma_j)} \right] \, . \tag{2.39b}$$

Here σ_j is defined in terms of μ in (2.32a), μ is defined in terms of λ in (2.21) and β_0 is defined in (2.30).

We make a few remarks concerning (2.39). Firstly, the dependence of χ_j in (2.39) on τ is strictly through the parameter $\mu = \sqrt{\tau\lambda/D}$, the importance of which will be discussed in the following section. From the explicit formula (2.32a), it follows that χ_j does not have a branch point at the origin $\lambda = 0$. Secondly, the spectrum of (2.39) is well known for the local eigenvalue problem corresponding to setting $\chi_j = 0$. In this case, it is known from [15] and [5] that, in addition to the zero eigenvalue associated with translation invariance, L_0 has a unique positive eigenvalue $\nu_0 = 5/4$ corresponding to an eigenfunction ϕ_0 of constant sign, and has an additional discrete eigenvalue on the negative real line at $\nu_2 = -3/4$.

Finally, the spectrum of the NLEP for (2.39) is recast into a more convenient form by first writing

$$\hat{\Phi} = \chi_j \left(\frac{\int_{-\infty}^{\infty} w\hat{\Phi}\, dy}{\int_{-\infty}^{\infty} w^2\, dy} \right) (L_0 - \lambda)^{-1} w^2 \,,$$

and then multiplying both sides of this equation by w and integrating over the real line. In this way we obtain that the eigenvalues of (2.39) are the roots of the transcendental equations $g_j(\lambda) = 0$, for $j = 0, \ldots, N-1$, where

$$g_j(\lambda) \equiv C_j(\lambda) - F(\lambda), \quad C_j(\lambda) \equiv \frac{1}{\chi_j(\lambda)}, \quad F(\lambda) \equiv \frac{\int_{-\infty}^{\infty} w\psi\, dy}{\int_{-\infty}^{\infty} w^2\, dy}, \quad \psi \equiv (L_0 - \lambda)^{-1} w^2. \quad (2.40)$$

2.3 Competition instabilities

In this section, we seek criteria in terms of D that guarantee that there is a positive real solution to (2.40) in the limit $\tau \to 0^+$. Such a root corresponds to an unstable real positive eigenvalue of the NLEP (2.39). For $\tau \to 0^+$ it will be shown that such a linear instability is of competition-type in the sense that it conserves the sum of the amplitudes of the spikes. The instability threshold condition on D will also be shown to apply to the case where $\tau > 0$.

We begin the analysis by recalling key properties of the function $F(\lambda)$ when λ is real and positive as determined in Proposition 3.5 of [32]. We then determine the behaviour of $C_j(\lambda)$ in (2.40) in the limit $\tau \to 0^+$. Using the properties of $C_j(\lambda)$ in this limit, together with the properties of $F(\lambda)$, we obtain criteria for which there exists a positive real value of λ at which $C_j(\lambda)$ and $F(\lambda)$ intersect. Some global properties of $F(\lambda)$ when λ is real and positive, which were rigorously established in [32], are as follows:

$$F(\lambda) > 0, \quad F'(\lambda) > 0, \quad F''(\lambda) > 0, \quad \text{for} \quad 0 < \lambda < 5/4\,; \quad F(\lambda) < 0, \quad \text{for} \quad \lambda > 5/4.$$
$$(2.41a)$$

Furthermore, since $L_0 w = w^2$ and the operator $(L_0 - \lambda)$ is not invertible at $\lambda = 5/4$, we obtain

$$F(0) = 1, \qquad F(\lambda) \to +\infty, \quad \text{as} \quad \lambda \to 5/4^-. \quad (2.41b)$$

To determine the behaviour of $C_j(\lambda)$ as $\tau \to 0^+$, we first write $C_j(\lambda)$ in terms of σ_j as

$$C_j(\lambda) = \frac{1}{2} \left[1 + \xi_j + \frac{f\xi_j}{1 + \lambda - f} \right]; \quad \xi_j = \frac{\mu\sigma_j}{\beta_0}, \quad j = 0, \ldots, N-1. \quad (2.42)$$

For any branch of $\sqrt{\lambda}$, this function is analytic in the finite λ plane except at the simple pole $\lambda = -1 + f$, which is on the negative real axis since $0 < f < 1$. Upon taking the limit $\mu \to 0^+$ in σ_j in (2.32a), we see that ξ_j in (2.42) has the behaviour

$$\xi_0 \to 0^+ \, ; \quad \xi_j \to \frac{Na_j}{\beta_0}, \quad a_j \equiv 1 - \cos\left(\frac{j\pi}{N}\right), \quad j = 1, \dots, N-1, \quad \text{as} \quad \tau \to 0^+, \quad (2.43)$$

where β_0 is defined in (2.30).

Firstly, by (2.43) and (2.42), we have that $C_0(\lambda) \equiv 1/2$ for all λ when $\tau = 0$. Thus, by (2.41), it follows that $g_0(\lambda) \neq 0$ for any $\lambda \geqslant 0$. Moreover, from the rigorous study of [34] (see Corollary 1.2 of [34]), we can conclude, more strongly, that when $C_0 = 1/2$ there are no roots to $g_0(\lambda) = 0$ in the unstable right half-plane $\text{Re}(\lambda) > 0$ (see (2.4)). Thus, the $(1, \dots, 1)^t$ mode, governing synchronous instabilities of the amplitudes of the spikes, is always stable in the limit $\tau \to 0^+$.

Next, consider the modes $j = 1, \dots, N-1$. Since ξ_j in (2.43) for $j > 0$ is independent of λ in the limit $\tau \to 0^+$, it follows from (2.42) that $C_j'(\lambda) < 0$ and $C_j(\lambda) > 0$ for $\lambda \geqslant 0$ when $j = 1, \dots, N-1$. Thus, from (2.41), we conclude that if $\max_j C_j(0) < 1$ for $j = 1, \dots, N-1$, there are no real positive eigenvalues when $\tau = 0$. A simple calculation using (2.42) and (2.43) shows that as $\tau \to 0^+$, we have the ordering $C_{N-1}(0) > C_{N-2}(0) > \dots > C_1(0)$. Therefore, in the limit $\tau \to 0^+$, (2.39) has no real positive eigenvalues when

$$C_{N-1}(0) = \frac{1}{2}\left[\frac{1 + \xi_{N-1} - f}{1 - f}\right] < 1. \quad (2.44)$$

If $C_{N-1}(0) > 1$, there is an unstable positive real eigenvalue when $\tau \to 0^+$. The threshold value D_{c_N} of D, as given below in (2.45), is obtained by setting $C_{N-1}(0) = 1$, and then using (2.43) for ξ_{N-1} together with (2.30) for β_0.

Although for the case $\tau > 0$ it is no longer true that $C_{N-1}(\lambda)$ is monotonically decreasing, we still have that $C_{N-1}(0) > 1$ when $D > D_{c_N}$. Hence, by the properties of $F(\lambda)$ given in (2.41) it follows that there must still be a positive root to $C_{N-1}(\lambda) = F(\lambda)$. However, when $\tau > 0$ it is possible that there can be further real positive roots where the other curves $C_j(\lambda)$ for $j = 0, \dots, N-2$ intersect $F(\lambda)$. We summarize our instability result as follows.

Principal Result 2.3 *Let $\epsilon \to 0$ and $\tau \geqslant 0$ in (1.3). Then the N-spike equilibrium solution ($N \geqslant 2$) constructed in Section 2.1 is unstable when*

$$D > D_{c_N} \equiv \frac{2f^2}{3N^3(1-f)\left(1 + \cos\frac{\pi}{N}\right)}, \quad 0 < f < 1, \quad (2.45)$$

and the spectrum of the NLEP (2.39) contains at least one unstable positive real eigenvalue. For $\tau \to 0^+$, the instability is of competition-type in the sense that any linearly unstable eigenvector v_j for the spike amplitudes must satisfy $(1, \dots, 1) \cdot v_j = 0$.

We now make some remarks. Firstly, for the limiting case $\tau \to 0^+$, in Section 2.4 a winding number calculation will be used to prove that there are no unstable complex eigenvalues in the right half-plane when $D < D_{c_N}$. Therefore, for $\tau \to 0^+$, the threshold D_{c_N} gives a necessary and sufficient condition for stability. Secondly, by comparing (2.45)

with (2.47), we see that as $\tau \to 0^+$, the N-spike equilibrium solution (2.15) is stable if and only if it is stable to small eigenvalues. Thirdly, the term competition instability is due to the fact that when such an instability is triggered, some spikes grow in amplitude while others decrease. This is due to the difference in signs of the components of the eigenvectors v_j for $j = 1, \ldots, N - 1$. As shown in the numerical experiments, computed from the full Brusselator model (1.3), this linear instability triggers a nonlinear event that leads to spike annihilation. In contrast, as was shown above, the synchronous mode corresponding to $v_0 = (1, \ldots, 1)^t$ is always stable when τ is sufficiently small. Fourthly, D_{c_N} decreases as $\sim N^{-3}$ when N is large, which is the same scaling as for the Schnakenberg model (Corollary 3.1 of [31]). In contrast, the GM (Proposition 7 of [9]) and GS [12] models have a more robust N^{-2} scaling in terms of the ability to support additional spikes. Since D is inversely proportional to the square length of the domain, (2.45) shows that in order to maintain stability the domain size must increase as the number of spikes increases. Finally, in terms of the original Brusselator parameters B_0, D_0 and E_0 in (1.6), we have the stability criterion

$$D_0 < D_{0c_N} \equiv \frac{2E_0^2 B_0^2}{3N^3(B_0 + 1)^{5/2}\left(1 + \cos\frac{\pi}{N}\right)}. \tag{2.46}$$

Thus, a spike pattern can be stabilized with small D_0 or large E_0. Note that, by (1.4), $E_0^2 = \mathcal{O}(\tau^{-1})$ so that $D_{0c_N} = \mathcal{O}(\tau^{-1})$ as $\tau \to 0^+$. However, if we require that $D = \mathcal{O}(1)$ with respect to τ, then D_0 must also be $\mathcal{O}(\tau^{-1})$ by (1.4). Also, if $\tau = (B_0 + 1)^{5/2}/E_0^2$ is held constant, then increasing B_0 in (2.46) relaxes the stability criterion. This fact is reflected in terms of the rescaled variables in (2.45), where increasing $f = B_0/(B_0 + 1)$ towards unity increases D_{c_N}.

Finally, we remark that the eigenvalue problem (2.17) admits another class of eigenvalues associated with translation-type instabilities, and these eigenvalues are of the order $\lambda = \mathcal{O}(\epsilon^2)$ as $\epsilon \to 0$. These eigenvalues, studied in [27], were found to be real negative when $\tau = \mathcal{O}(1)$ if and only if $D < D_{s_N}$, where (cf. [27])

$$D_{s_N} \equiv \frac{f^2}{3N^3(1 - f)} < D_{c_N}. \tag{2.47}$$

This threshold value is the same as that calculated in (2.16) for the bifurcation point corresponding to the emergence of asymmetric N-spike equilibria from a symmetric N-spike equilibrium solution branch.

2.4 Complex eigenvalues and oscillatory instabilities

For the case $D < D_{c_N}$ and $\tau = 0$, we now use a winding number argument to prove that (2.39) has no unstable eigenvalues with $\text{Re}(\lambda) > 0$. To calculate the number of zeros of $g_j(\lambda)$ in the right half-plane, we compute the winding of $g_j(\lambda)$ over the contour Γ traversed in the counterclockwise direction composed of the following segments in the complex λ-plane: Γ_I^+ ($0 < \text{Im}(\lambda) < iR$, $\text{Re}(\lambda) = 0$), Γ_I^- ($-iR < \text{Im}(\lambda) < 0$, $\text{Re}(\lambda) = 0$), and Γ_R is the semi-circle in the right half-plane defined by $|\lambda| = R > 0$, $-\pi/2 < \arg(\lambda) < \pi/2$, where $R > 0$.

Each function $g_j(\lambda)$ in (2.40) for $j = 0,\ldots,N-1$ is analytic in $\text{Re}(\lambda) \geqslant 0$ except at the simple pole $\lambda = 5/4$ corresponding to the unique positive eigenvalue of the operator L_0 in (2.28). Therefore, by the argument principle we obtain that $M_j - 1 = (2\pi)^{-1}\lim_{R\to\infty}[\arg g_j]_{\Gamma}$, where M_j is the number of zeros of g_j in the right half-plane, and where $[\arg g_j]_{\Gamma}$ denotes the change in the argument of g_j over Γ. Furthermore, from (2.40), (2.42) and (2.43) it follows that $g_j \to (1+\xi_j)/2$ as $|\lambda| \to \infty$ on the semi-circle Γ_R so that $\lim_{R\to\infty}[\arg g_j]_{\Gamma_R} = 0$. For the contour Γ_I^-, we use $g_j(\bar{\lambda}) = \overline{g_j(\lambda)}$ so that $[\arg g_j]_{\Gamma_I^-} = [\arg g_j]_{\Gamma_I^+}$. By summing the roots of the N separate functions $g_j(\lambda)$ for $j = 0,\ldots,N-1$, we obtain that the number M of unstable eigenvalues of the NLEP (2.39) when $\tau = 0$ is

$$M = N + \frac{1}{\pi}\sum_{j=0}^{N-1}\left[\arg g_j\right]_{\Gamma_I^+}. \tag{2.48}$$

Here $[\arg g_j]_{\Gamma_I^+}$ denotes the change in the argument of g_j as the imaginary axis $\lambda = i\lambda_I$ is traversed from $\lambda_I = +\infty$ to $\lambda_I = 0$.

To calculate $[\arg g_j]_{\Gamma_I^+}$ when $\tau = 0$, we substitute $\lambda = i\lambda_I$ into (2.42) for C_j, and separate the resulting expression into real and imaginary parts to obtain

$$C_j(i\lambda_I) = C_{jR}(\lambda_I) + iC_{jI}(\lambda_I), \tag{2.49a}$$

where

$$C_{0R}(\lambda_I) = \frac{1}{2}, \quad C_{0I}(\lambda_I) = 0, \tag{2.49b}$$

$$C_{jR}(\lambda_I) = \frac{1}{2}\left[1 + \xi_j + \frac{f\xi_j(1-f)}{(1-f)^2 + \lambda_I^2}\right], \quad C_{jI}(\lambda_I) = -\frac{f\xi_j\lambda_I}{(1-f)^2 + \lambda_I^2}, \quad j = 1,\ldots,N-1. \tag{2.49c}$$

In (2.49) we use the limiting behaviour for ξ_j as $\tau \to 0^+$ as given in (2.43).

Similarly, we separate the real and imaginary parts of $F(i\lambda_I)$, where $F(\lambda)$ was defined in (2.40) to obtain

$$F(i\lambda_I) = \frac{\int_{-\infty}^{\infty}wL_0\left[L_0^2 + \lambda_I^2\right]^{-1}w^2\,dy}{\int_{-\infty}^{\infty}w^2\,dy} + i\left(\frac{\lambda_I\int_{-\infty}^{\infty}w\left[L_0^2 + \lambda_I^2\right]^{-1}w^2\,dy}{\int_{-\infty}^{\infty}w^2\,dy}\right) \equiv F_R(\lambda_I) + iF_I(\lambda_I), \tag{2.50}$$

which determines $g(i\lambda_I)$ from (2.40) as

$$g_j(i\lambda_I) = C_{jR}(\lambda_I) - F_R(\lambda_I) + i\left[C_{jI}(\lambda_I) - F_I(\lambda_I)\right] \equiv g_{jR}(\lambda_I) + ig_{jI}(\lambda_I). \tag{2.51}$$

In order to calculate $[\arg g_j]_{\Gamma_I^+}$, we require the following properties of $F_R(\lambda_I)$ and $F_I(\lambda_I)$ as established rigorously in Propositions 3.1 and 3.2 of [32]:

$$F_R(0) = 1; \quad F_R'(\lambda_I) < 0, \quad \lambda_I > 0; \quad F_R(\lambda_I) = \mathcal{O}(\lambda_I^{-2}), \quad \lambda_I \to +\infty, \tag{2.52a}$$

$$F_I(0) = 0; \quad F_I(\lambda_I) > 0, \quad \lambda_I > 0; \quad F_I(\lambda_I) = \mathcal{O}(\lambda_I^{-1}), \quad \lambda_I \to +\infty. \tag{2.52b}$$

By using (2.49) and (2.52), we obtain from (2.51) that $g_{0R} < 0$ and $g_{0I} = 0$ at $\lambda_I = 0$, while $g_{0R} > 0$ and $g_{I0} = 0$ as $\lambda_I \to +\infty$. In addition, since $F_I(\lambda_I) > 0$, we conclude that

$g_{0I} < 0$ for $\lambda_I > 0$. Therefore, $[\arg g_0]_{\Gamma_I^+} = -\pi$, and hence (2.48) becomes

$$M = N - 1 + \frac{1}{\pi} \sum_{j=1}^{N-1} [\arg g_j]_{\Gamma_I^+}. \tag{2.53}$$

The calculation of $[\arg g_j]_{\Gamma_I^+}$ for $j = 1, \dots, N-1$ is similar, but depends on the range of D. Suppose that $D < D_{c_N}$, where D_{c_N} is the threshold of (2.45) so that $C_{jR}(0) < 1$ for all $j = 1, \dots, N-1$. Then, from (2.49), (2.52) and (2.51), we calculate that $g_{0R} < 0$ and $g_{0I} = 0$ at $\lambda_I = 0$, while $g_{0R} > 0$ and $g_{I0} = 0$ as $\lambda_I \to +\infty$. In addition, since $F_I(\lambda_I) > 0$ and $C_{0I}(\lambda_I) < 0$, we get $g_{0I} < 0$ for all $\lambda_I > 0$. This gives $[\arg g_j]_{\Gamma_I^+} = -\pi$ for $j = 1, \dots, N-1$. From (2.53), we then obtain the following result:

Principal Result 2.4 *Let $\tau \to 0^+$ and $\epsilon \to 0$. Then, when $D < D_{c_N}$, where D_{c_N} is the threshold of (2.45), the NLEP (2.39) has no unstable eigenvalues in $\mathrm{Re}(\lambda) > 0$. Therefore, for $\tau \to 0^+$, the threshold D_{c_N} gives a necessary and sufficient condition for the stability of the N-spike equilibrium solution (2.15a) of (1.3).*

We remark that as D is increased above the threshold D_{c_N} in such a way that $C_{N-1}(0) > 1$ but $C_j(0) < 0$ for $j = 1, \dots, N-2$, we readily calculate from (2.49), (2.52) and (2.51) that $[\arg g_{N-1}]_{\Gamma_I^+} = 0$ and $[\arg g_j]_{\Gamma_I^+} = -\pi$ for $j = 1, \dots, N-2$. Therefore, from (2.53) we conclude that $M = 1$, and the only eigenvalue entering the right half-plane is the real eigenvalue corresponding to the competition instability analysed in Section 2.3. We remark that since τ appears only through the factor $\tau\lambda$, increasing τ cannot result in a competition instability. Thus, the threshold criterion (2.45) for stability is also valid for a range of $0 < \tau < \tau_0$ for some $\tau_0 > 0$ to be determined.

Next, we show that for $0 < D < D_{c_N}$, there are exactly $2N$ unstable eigenvalues in $\mathrm{Re}(\lambda) > 0$ when $\tau > 0$ is sufficiently large, and that these eigenvalues are on the positive real axis in $0 < \lambda < 5/4$. For $\tau \gg 1$, we obtain from (2.42) and (2.32a) that $C_j = \mathcal{O}(\sqrt{\lambda\tau})$ on Γ_R so that $\lim_{R \to \infty} [\arg g_j]_{\Gamma_R} = \pi/2$. In this way we obtain in place of (2.48),

$$M = \frac{5N}{4} + \frac{1}{\pi} \sum_{j=0}^{N-1} [\arg g_j]_{\Gamma_I^+}. \tag{2.54}$$

For $\tau \gg 1$ and $\lambda = i\lambda_I$, we obtain from (2.42) and (2.32a),

$$C_j = \frac{1}{2}\left[1 + \kappa\sqrt{i\tau\lambda_I} + \frac{f\kappa\sqrt{i\tau\lambda_I}}{1 - f + i\lambda_I}\right], \qquad \kappa \equiv \frac{2}{\beta_0\sqrt{D}}. \tag{2.55}$$

Separating into real and imaginary parts, with $C_j = C_{jR} + iC_{jI}$, we get for $\tau \gg 1$ and $\lambda_I \neq 0$,

$$
\begin{aligned}
C_{jR} &= \frac{\kappa\sqrt{\tau\lambda_I}}{2} \frac{|1 + i\lambda_I|}{|(1-f) + i\lambda_I|} \cos\left(\frac{\pi}{4} + \theta_0 - \theta_1\right) + \frac{1}{2}, \\
C_{jI} &= \frac{\kappa\sqrt{\tau\lambda_I}}{2} \frac{|1 + i\lambda_I|}{|(1-f) + i\lambda_I|} \sin\left(\frac{\pi}{4} + \theta_0 - \theta_1\right),
\end{aligned}
\tag{2.56a}
$$

where θ_0 and θ_1 are defined by

$$\theta_0 = \arctan(\lambda_I), \qquad \theta_1 = \arctan(\lambda_I/(1-f)). \tag{2.56b}$$

Since $\lambda_I > 0$, and $0 < f < 1$, then $0 < \theta_0 < \theta_1 < \pi/2$. Note that $C_{jR} > 0$ for any $\lambda_I > 0$ on this range of θ_0 and θ_1.

For $\tau \gg 1$, we have $g_j \sim c e^{i\pi/4}\sqrt{\lambda_I}$, where $c > 0$ is a real constant as $\lambda_I \to +\infty$. Therefore, we have $\arg(g_j) = \pi/4$ as $\lambda_I \to +\infty$. Now for $\lambda_I = 0$, we have $g_{jR} < 0$ and $g_{jI} = 0$ when $D < D_{c_N}$ so that $\arg(g_j) = \pi$ when $\lambda_I = 0$. In order to prove that $[\arg g_j]_{\Gamma_I^+} = 3\pi/4$, we must show that $g_{jI} > 0$ whenever $g_{Rj} = 0$. Since $F_R > 0$ and $C_{jR}(\lambda_I) > 0$ for $\lambda_I > 0$, but $C_{jR} = \mathcal{O}(\sqrt{\tau}) \gg 1$ for $\tau \gg 1$, it follows that any root λ_I^* of $g_{Rj} = 0$ must be such that $\lambda_I^* = \mathcal{O}(\tau^{-1}) \ll 1$. Thus, for $\tau \gg 1$, we have $\theta_0 \to 0$ and $\theta_1 \to 0$ as $\lambda_I \to 0$, and so we conclude from (2.56) that $C_{jI} > 0$ with $C_{jI} = \mathcal{O}(1)$ at $\lambda_I^* = \mathcal{O}(\tau^{-1})$. Finally, since $g_{jI} = C_{jI} - F_I$, and $F_I(0) = 0$, we conclude that $g_{jI} > 0$ at any root $\lambda_I^* \ll 1$ of $g_{jR} = 0$. This proves that $[\arg g_j]_{\Gamma_I^+} = 3\pi/4$ for each $j = 0, \ldots, N-1$. Finally, from (2.54) we conclude that $M = 2N$.

To determine more precisely the location of these unstable eigenvalues, we proceed as in Section 2.3. For $\tau \gg 1$, and on the positive real axis in $0 < \lambda < 5/4$, we obtain from (2.42) and (2.32a) that $C_j(\lambda)$ is a concave monotone increasing function. Since $C_j(0) < F(0) = 1$ when $D < D_{c_N}$ for $j = 0, \ldots, N-1$, it follows from the properties of $F(\lambda)$ in (2.41) that for each j, $C_j(\lambda) = F(\lambda)$ must have two roots on the interval $0 < \lambda < 5/4$. We summarize the result as follows.

Principal Result 2.5 *Let $\tau \to \infty$ and $\epsilon \to 0$. Then, when $0 < D < D_{c_N}$, where D_{c_N} is the threshold of* (2.45)*, the NLEP* (2.39) *has exactly $2N$ unstable eigenvalues in $Re(\lambda) > 0$. These eigenvalues are located on the real axis in the interval $0 < \lambda < 5/4$.*

Therefore, for the parameter range $0 < D < D_{c_N}$, and by the continuity of the branches of eigenvalues with respect to τ, we conclude that for each $j = 0, \ldots N-1$, there must be a minimum value $\tau_{0j} > 0$ of τ for which the NLEP (2.39) has a complex conjugate pair of eigenvalues at $\lambda = \pm i\lambda_{Ij}^0$, corresponding to each eigenmode in (2.32c). We define the oscillatory stability threshold τ_0 as the minimum of these thresholds, i.e. $\tau_0 = \min_j \tau_{0j}$. Our numerical results show that τ_0 is a Hopf bifurcation point, in the sense that an unstable complex conjugate pair of eigenvalues enters the right half-plane for τ slightly above τ_0. From (2.32c) the $j = 0$ mode corresponds to synchronous spike amplitude oscillations, while the other modes correspond to asynchronous oscillations in the spike amplitudes. For the GM model, as studied in [32], an ordering principle $\tau_{0j} < \tau_{0j+1}$, $j = 0, \ldots, N-2$ was observed for all values of the parameters tested. That is, the dominant oscillatory instability is that of synchronous oscillations of the spike amplitudes. In contrast, for all values of the parameter f tested, we find an interval of D in $0 < D < D_{c_N}$ in which this ordering principle is reversed. Thus, the Brusselator admits asynchronous oscillations not observed in previous studies of the stability of spike solutions. We conjecture that this is due to the activator acting as two separate sources for the inhibitor, necessitating the manipulation (2.37) to obtain the multiplier of the non-local term in the NLEP (2.38). We

(a) $\tau_{0j}(D)$ for $N = 2$ (b) $\tau_{0j}(D)$ for $N = 2$ closeup   (c) $\lambda_{Ij}^0(D)$ for $N = 2$
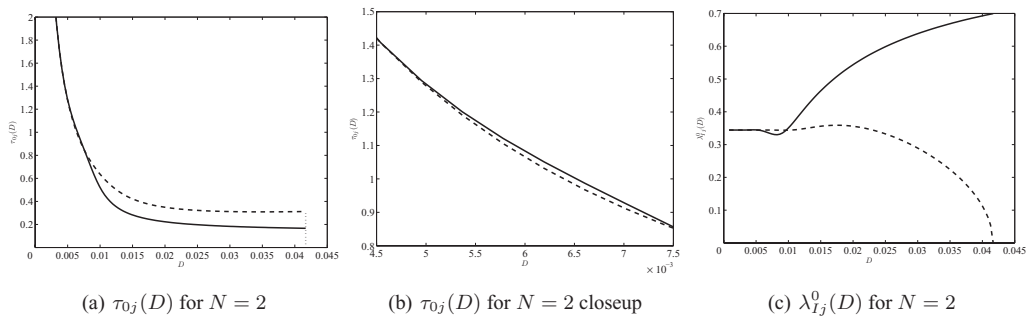
FIGURE 2. Plots of $\tau_{0j}(D)$ (left and centre figures) and $\lambda_{Ij}^0(D)$ (right figure) for $N = 2$ and $f = 0.5$. The critical value $D_{c2} \approx 0.0417$ is indicated by the vertical dotted line. In all figures, the solid and dashed curves correspond to $j = 0$ and $j = 1$, respectively. In the magnified interval shown in the centre figure, $\tau_{01} < \tau_{00}$, indicating the possibility of asynchronous oscillations.

illustrate asynchronous oscillatory phenomena for two-, three- and four-spike examples in Section 2.5.

To determine the smallest value τ_{0j} for which there are two eigenvalues $\lambda = \pm i\lambda_{Ij}^0$ with $\lambda_{Ij}^0 > 0$, on the imaginary axis, and no eigenvalues in the right half-plane, we solve the coupled system $g_{Rj} = g_{Ij} = 0$ given in (2.51) for τ_{0j} and λ_{Ij}^0. In (2.51), $C_{jR}(\lambda_I) = \mathrm{Re}(C_j(i\lambda_I))$ and $C_{jI}(\lambda_I) = \mathrm{Im}(C_j(i\lambda_I))$, where $C_j(\lambda)$ is defined in (2.42) in terms of σ_j as given in (2.32a). The critical value τ_0 is then defined by

$$\tau_0 = \min_j \tau_{0j}. \tag{2.57}$$

For given parameters D and f, we used the MATLAB function fsolve() to solve the system $g_{Rj} = g_{Ij} = 0$ for τ_{0j} and λ_{Ij}^0. To evaluate $F_R(\lambda_I)$ and $F_I(\lambda_I)$ in (2.50), we discretized the operator $[L_0^2 + \lambda_I^2]$ over the interval $-20 < y < 20$ using 500 grid points and used MATLAB's inversion algorithm to solve the boundary value problem. The trapezoidal rule was used to evaluate the integrals in $F_R(\lambda_I)$ and $F_I(\lambda_I)$. Halving the number of grid points, or halving the interval length, did not significantly affect the calculated values of $F_R(\lambda_I)$ and $F_I(\lambda_I)$. In all subsequent plots of τ_{0j} and λ_{Ij}^0, we treat D as the bifurcation parameter and hold f fixed at a particular value. For the values of f tested in the interval $0 < f < 1$, the qualitative behaviour of $\tau_{0j}(D)$ remained unchanged.

In Figure 2(a), we plot the curves $\tau_{0j}(D)$ for $N = 2$ and $f = 0.5$. The critical value D_{c2} is indicated by the vertical dotted line in the figure. When $D = D_{c2}$, the $j = 1$ curve ends as the corresponding pair of imaginary eigenvalues meet at the origin, as shown in the plot of $\lambda_{Ij}^0(D)$ in Figure 2(c). As D increases above D_{c2}, one eigenvalue moves on the real axis into the right half-plane. Because the $j = 0$ mode does not undergo such a bifurcation, the $j = 0$ curve continues beyond D_{c2} but is not plotted. In general, the jth curve ends when the jth mode becomes unstable to a real eigenvalue crossing into the right half-plane from the origin. In Figure 2(b), we magnify the interval given in Figure 2(a) where the ordering principle $\tau_{01} < \tau_{00}$ holds. For D in this interval, we expect asynchronous oscillations to be the dominant instability. For D to the right of this interval, the familiar ordering principle $\tau_{00} < \tau_{01}$, guaranteeing synchronous oscillatory instabilities, is restored.
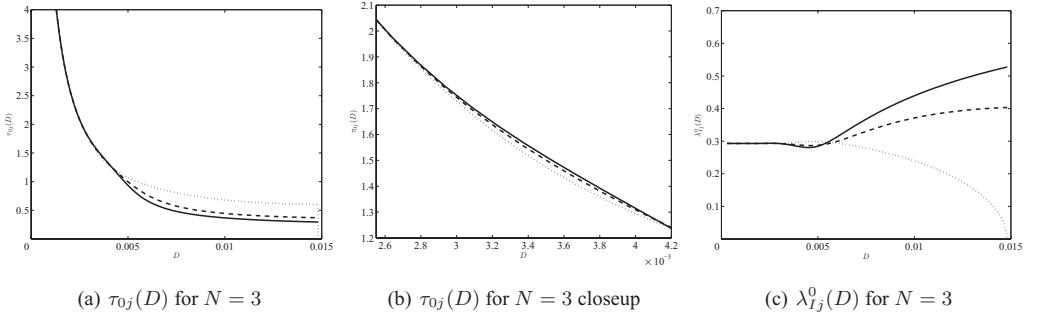
(a) $\tau_{0j}(D)$ for $N = 3$ (b) $\tau_{0j}(D)$ for $N = 3$ closeup   (c) $\lambda_{Ij}^0(D)$ for $N = 3$

FIGURE 3. Plots of $\tau_{0j}(D)$ (left and centre figures) and $\lambda_{Ij}^0(D)$ (right figure) for $N = 3$ and $f = 0.6$. The critical value $D_{c3} \approx 0.0148$ is indicated by the vertical dotted line. In all figures, the solid, dashed and dotted curves correspond to $j = 0, 1, 2$, respectively. In the magnified interval shown in the centre figure, $\tau_{02} < \tau_{01} < \tau_{00}$.
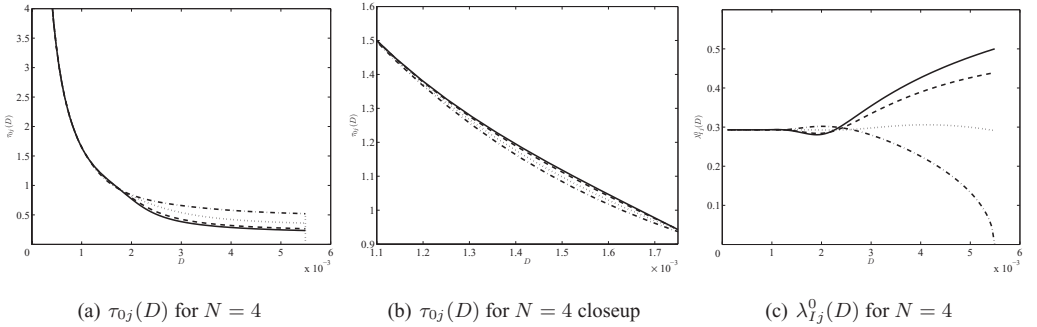

(a) $\tau_{0j}(D)$ for $N = 4$ (b) $\tau_{0j}(D)$ for $N = 4$ closeup   (c) $\lambda_{Ij}^0(D)$ for $N = 4$

FIGURE 4. Plots of $\tau_{0j}(D)$ (left and centre figures) and $\lambda_{Ij}^0(D)$ (right figure) for $N = 4$ and $f = 0.6$. The critical value $D_{c4} \approx 0.0055$ is indicated by the vertical dotted line. In all figures, the solid, dashed, dotted, and dash-dotted curves correspond to $j = 0, 1, 2, 3$, respectively. In the magnified interval shown in the centre figure, $\tau_{03} < \tau_{02} < \tau_{01} < \tau_{00}$.

In Figure 3(a), we show a plot of $\tau_{0j}(D)$ for a three-spike example with $f = 0.6$. We again plot only the interval $0 < D < D_{c3}$ above which the $j = 2$ curve ceases to exist. In the plot of $\lambda_{Ij}^0(D)$ in Figure 3(c), we see that $\lambda_{I2}^0 \to 0$ as $D \to D_{c3}^-$. In Figure 3(b), the reverse ordering principle is again observed for an interval of D, indicating the possibility of asynchronous oscillations. As similar to the previous two-spike case, for D to the right of this interval, the usual ordering principle guaranteeing synchronous oscillatory instabilities is restored. The same characteristics of $\tau_{0j}(D)$ and $\lambda_{Ij}^0(D)$ for a four-spike example with $f = 0.6$ are seen in Figures 4(a)–(c).

For the two-spike example of Figure 2 with $f = 0.5$, we trace the paths of the pair of complex conjugate eigenvalues in the right half-plane as τ increases past the Hopf bifurcation value computed in Figures 2(a) and (b). For the two modes $j = 0$ (Figure 5(a)) and $j = 1$ (Figure 5(b)), we start with the pair $(\tau, \lambda) = (\tau_{0j}(D), \lambda_{Ij}^0)$ and solve $g(\lambda) = 0$ in (2.40) for increasingly larger values of τ. For the $j = 0$ mode, we take $D = 0.03$ whereas for the $j = 1$ mode, we take $D = 0.006$ so that in both cases the eigenvalues being tracked are the first ones to cross into the right half-plane. The eigenvalues converge onto the

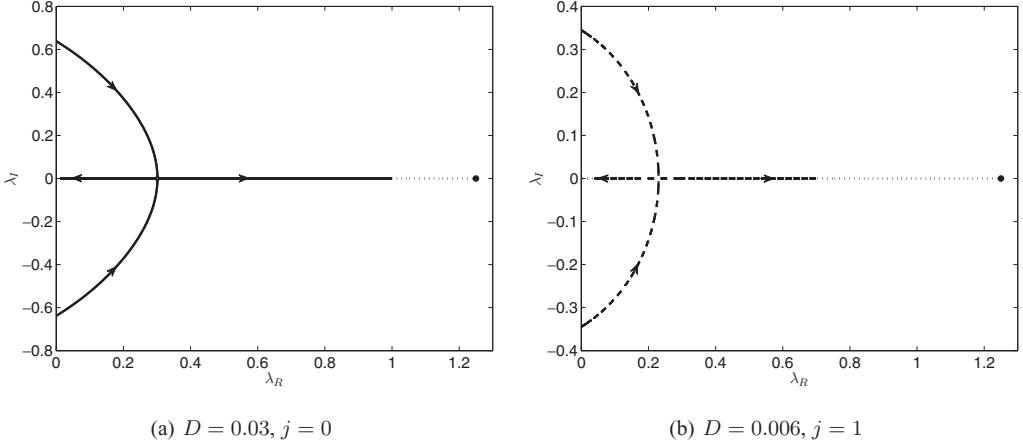(a) $D = 0.03$, $j = 0$ (b) $D = 0.006$, $j = 1$

FIGURE 5. Plots of the paths of $\lambda = \lambda_I + i\lambda_R$ with $N = 2$, and $f = 0.5$ for $(D, j) = (0.03, 0)$ (left) and $(D, j) = (0.006, 1)$ (right) as τ increases past its Hopf bifurcation value $\tau_{0j}(D)$. The arrows denote the direction of traversal for increasing τ. The eigenvalues converge onto the positive real axis when τ reaches some value $\tau_c(D) > \tau_{0j}(D)$. The eigenvalues split, with one tending to 0 and the other tending to $v_0 = 5/4$ as $\tau \to \infty$, where v_0 is the unique positive eigenvalue of the operator L_0.

positive real axis when τ is sufficiently large. As τ is increased further, the eigenvalues split and migrate along the positive axis towards 0 and $v_0 = 5/4$ as $\tau \to \infty$, where v_0 is the principal eigenvalue of the operator L_0.

Key characteristics shared by Figures 2–4 are the behavior of τ_{0j} and λ_{Ij}^0 for small values of D. These figures suggest that $\tau_{0j} \to \infty$, while λ_{Ij}^0 approaches a constant value also independent of j. We now provide a simple analytical explanation for this limiting behaviour. We remark that this unbounded behaviour of τ_{0j} as $D \to 0$ is in marked contrast to the finite limiting behaviour as obtained in [12] or [32] for the GS and GM RD models, respectively.

In the limit $D \to 0$, a simple scaling argument shows that $|\mu| \to \infty$, where $\mu = \sqrt{\tau\lambda/D}$. We then readily obtain from (2.32a) that $\sigma_j \to 2$ as $D \to 0$ and that $\beta_0 = \mathcal{O}(D^{-1})$. Therefore, from (2.42), we get the limiting behaviour,

$$C_j \sim C \equiv \frac{1}{2}\left[1 + \alpha z \sqrt{\lambda} + \frac{\alpha f z \sqrt{\lambda}}{1 - f + \lambda}\right], \quad z = \sqrt{\tau D}, \quad \alpha = \frac{\alpha^2 v_c^2}{3}, \quad j = 0, \ldots, N-1.$$

(2.58)

We set $\lambda = i\lambda_I$, where $\lambda_I > 0$, and then separate (2.58) into real and imaginary parts to get

$$C \equiv C_R(\lambda_I) + iC_I(\lambda_I) \equiv \frac{1}{2}\left[1 + \frac{\alpha z}{\sqrt{2}}\sqrt{\lambda_I}M_+\right] + i\frac{1}{2\sqrt{2}}\alpha z\sqrt{\lambda_I}M_-; \quad M_\pm \equiv \frac{1 - f \pm \lambda_I f + \lambda_I^2}{(1-f)^2 + \lambda_I^2}.$$

(2.59)

Since C is independent of j, it follows that the root $\tau = \tau_{0l}$ and $\lambda_I = \lambda_{Il}$ to the limiting coupled system $C_R(\lambda_I) = F_R(\lambda_I)$ and $C_I(\lambda_I) = F_I(\lambda_I)$ must be independent of j.

For this coupled system to possess a root, it is readily seen that we must have $z = \sqrt{\tau D} = \mathcal{O}(1)$ as $D \to 0$, which implies that $\tau_{0l} = \mathcal{O}(D^{-1})$ as $D \to 0$. We use (2.59) to eliminate z between the coupled system $C_R(\lambda_I) = F_R(\lambda_I)$ and $C_I(\lambda_I) = F_I(\lambda_I)$. In this way we obtain that λ_{Il} must be a root of

$$H_R(\lambda_I) = H_I(\lambda_I), \tag{2.60a}$$

where $H_R(\lambda_I)$ and $H_I(\lambda_I)$ are defined by

$$H_R(\lambda_I) = \frac{2F_R(\lambda_I) - 1}{\lambda_I^2 + f\lambda_I + 1 - f}, \quad H_I = \frac{2F_I(\lambda_I)}{\lambda_I^2 - f\lambda_I + 1 - f}. \tag{2.60b}$$

Therefore, for $D \to 0$, we conclude that λ_{Il} depends only on f and is independent of N. The scaling $\tau_{0l} = \mathcal{O}(D^{-1})$ was not observed in the analysis of the GS [12] or GM models [32].

We now prove the existence of a solution $\lambda_{Il} > 0$ to (2.60). We begin by noting that $H_R(0) = (1 - f)^{-1} > 0$ and that $H_R(\lambda_I)$ has no poles when $\lambda_I \geqslant 0$. Also, because $F_R \to 0$ as $\lambda_I \to \infty$, we find from (2.60b) that $H_R \sim -1/\lambda_I^2 < 0$ as $\lambda_I \to \infty$. To show the existence of an intersection between H_R and H_I, there are two cases to consider. The first case is when $0 < f < 2(\sqrt{2} - 1)$ so that the denominator of H_I is always positive. Since $F_I(0) = 0 < F_R(0) = 1$, and $F_I(\lambda_I) > 0$ for $\lambda_I > 0$, then by the properties of H_R there must exist a solution to (2.60a). When $2(\sqrt{2} - 1) < f < 1$, $H_I(\lambda_I)$ has two poles on the positive real axis at $\lambda_I = \lambda_I^{l,r}$ ordered $0 < \lambda_I^l < \lambda_I^r$ with $\lambda_I^l \to 0^+$ as $f \to 1^-$. Therefore, $H_I \to +\infty$ as $\lambda_I \to \lambda_I^{l-}$. Because $H_R(0) > 0$ and is bounded for all λ_I while $H_I(0) = 0$, there must exist a solution to (2.60a) on the interval $0 < \lambda_I < \lambda_I^l$. This completes the proof of the existence of a root $\lambda_{Il} > 0$ under the scaling $\tau = \mathcal{O}(D^{-1})$ as $D \to 0$. While we have not been able to show analytically that λ_{Il} is unique, we have not observed numerically an example that yields more than one solution to (2.60a).

In Figure 6(a), we show the log–log relationship between τ_{0j} and small D for the examples shown in Figures 2–4. Note that in each case, all curves corresponding to modes $j = 0, \ldots, N - 1$ are plotted. However, as stated above, τ_{0j} is independent of j for small D and thus the curves are indistinguishable in the plot. In Figure 6(b), we plot N curves of λ_{Ij}^0 as a function of f with D small for $N = 2, 3, 4$. We also plot the solution to (2.60a). Although for each value of N we use a different value of D specified as $D = D_{cN}/10$, all curves are indistinguishable at the resolution allowed by the figure. Because $\lambda_I^l \to 0^+$ as $f \to 1^-$, we expect theoretically that $\lambda_{Il} \to 0^+$ in this limit. Numerically, however, the problem (2.60a) for $1 - f$ small becomes ill-conditioned and our numerical solver fails when f is too close to $f = 1$.

The main limitation of our analysis is that we are unable to determine whether, for each function g_j, a complex conjugate pair of pure imaginary eigenvalues exists at only one value of τ_{0j} for all the ranges of the parameters. Our numerical experiments suggest that for $0 < \tau < \tau_{0j}$ and $D < D_{0cN}$, the pattern is stable. This indicates that our computed thresholds τ_{0j} are the minimum values of τ for which an oscillatory instability occurs.

One possible way to obtain a rigorous bound on τ_{0j} is to use the following inequality, as derived in equation (2.29) of [33] (see also equation (5.62) of [35]), for any eigenvalue
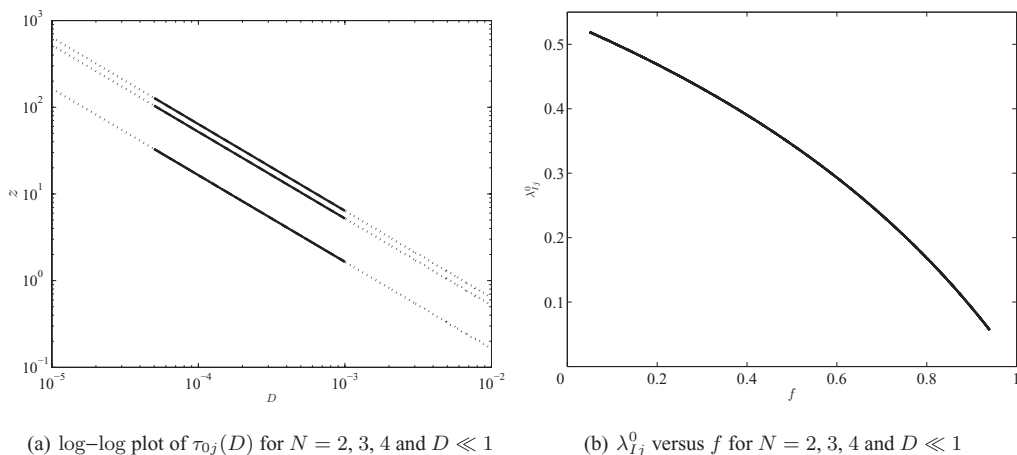
(a) log–log plot of $\tau_{0j}(D)$ for $N = 2, 3, 4$ and $D \ll 1$

(b) λ_{Ij}^0 versus f for $N = 2, 3, 4$ and $D \ll 1$

FIGURE 6. The log–log relationship between τ_{0j} and small D with parameters from Figures 2–4 (left), and λ_{Ij}^0 versus f with D small for $N = 2, 3, 4$ (right). In the left figure, the solid lines are numerically computed solutions of $\tilde{g}_{Rj} = \tilde{g}_{Ij} = 0$, while all the dotted lines have slope -1. The top line corresponds to $N = 2$, $f = 0.5$, the centre line to $N = 3$, $f = 0.6$ and the bottom line corresponds to $N = 4$ and $f = 0.6$. Different curves of each example corresponding to modes $j = 0, \ldots, N-1$ are indistinguishable. In the right figure, the curves of λ_{Ij}^0 versus f generated by the solution to $\tilde{g}_{Rj} = \tilde{g}_{Ij} = 0$ are plotted, as is the solution to (2.60a). These curves are indistinguishable at the resolution allowed by the figure.

λ of the NLEP of (2.39) with multiplier χ_j:

$$|\chi_j - 1|^2 + \operatorname{Re}\left(\bar{\lambda}\chi_j\right)\left(\frac{\int_{-\infty}^{\infty} w^2\, dy}{\int_{-\infty}^{\infty} w^3\, dy}\right) \leqslant 0. \tag{2.61}$$

Upon evaluating the integral ratio, and then using $\chi_j = 1/C_j$ and $\operatorname{Re}(\bar{z}) = \operatorname{Re}(z)$, we obtain that (2.61) reduces to

$$|C_j - 1|^2 + \frac{5}{6}\operatorname{Re}(\lambda C_j) \leqslant 0. \tag{2.62}$$

For RD systems in [33] and Section 5 of [35] for which C_j is a simple rational function of λ, (2.62) was used successfully to obtain a rigorous bound on the Hopf bifurcation threshold of τ. However, for the Brusselator, C_j in (2.42) is not rational in λ, and it is not clear how to use (2.62) to obtain an explicit analytical bound on the Hopf bifurcation threshold τ_{0j}.

2.5 Numerical validation

Next, we illustrate the theory presented in Sections 2.3 and 2.4 regarding competition and oscillatory instabilities of N-spike equilibria. We solve the Brusselator model without boundary flux (1.3) numerically using the MATLAB partial differential equations solver

pdepe() with non-uniformly spaced grid points distributed according to the mapping,

$$y = x + \sum_{i=0}^{N-1} \tanh\left[\frac{x - x_i}{2\epsilon}\right]; \quad -1 - N < y < 1 + N,$$

where x is the physical grid. The initial conditions were taken to be a perturbation of the equilibrium spike solution of the form

$$u(x,0) = u_e^*(x)\left[1 + \delta \sum_{k=0}^{N-1} d_k e^{-(x-x_k)^2/(4\epsilon^2)}\right], \quad v(x,0) = v_e^*(x), \qquad (2.63)$$

where $\delta \ll 1$ is taken to be 0.002, and d_k is the $(k+1)$th component of the vector $\boldsymbol{d}$ to be defined below. Either 2000 ($\epsilon = 0.005$) or 4000 ($\epsilon = 0.001$) grid points were used to produce the numerical results below. In (2.63), instead of u_e, v_e given in (2.15), we use the true equilibrium u_e^*, v_e^* calculated using small τ starting from the initial conditions u_e, v_e. Because τ does not influence the equilibrium solution, u_e^*, v_e^* may be used as valid initial conditions for any value of τ. We briefly explain the reason for this procedure. With an insufficiently small choice for τ while starting with u_e and v_e as initial conditions, we observe an immediate annihilation of one or more of the spikes. We conjecture that this is due to the inaccuracy of the asymptotic solution associated with the non-zero background of the activator, coupled with the sluggish response of the inhibitor. However, for τ sufficiently small, the inhibitor is able to respond quickly to prevent an annihilation, allowing the system to evolve to a spike equilibrium state u_e^*, v_e^*.

In (2.63), the choice of the vector $\boldsymbol{d}$ depends on the phenomenon that we illustrate. In computations illustrating competition instabilities, $\boldsymbol{d}$ is taken to be a multiple of v_{N-1}, the eigenvector given in (2.32c) associated with the eigenvalue that first crosses into the right half-plane as D is increased above D_{cN} when τ is sufficiently small. The values of D in the experiments illustrating competition instabilities will be such that only the $j = N - 1$ mode is unstable. In computations illustrating oscillatory instabilities, $\boldsymbol{d}$ is taken to be a multiple of the vector $\sum_{j=0}^{N-1} v_j$, with v_j given in (2.32c), which allows for all the modes to be present initially. We track the evolution of the modes through the quantity b_j^{amp}, defined as the amplitude of the oscillations of b_j given by

$$b_j = |\Delta\boldsymbol{u}_m^t v_j|, \quad \Delta\boldsymbol{u}_m \equiv (u_{m0} - u_e^*(x_0, 0), \ldots, u_{mN-1} - u_e^*(x_{N-1}, 0))^t; \quad j = 0, \ldots, N-1, \quad (2.64)$$

allowing clear identification of which modes grow or decay. Here u_{mn} denotes the numerically computed solution at the jth equilibrium spike location defined by $u_{mj} \equiv u(x_j, t)$ where $x_j = -1 + (2j + 1)/N$ with $j = 0, \ldots, N - 1$. In all experiments, $\boldsymbol{d}$ is normalized so that $\max_k d_k = 1$.

We consider three experiments with two, three and four spikes. In each experiment f is fixed, while different combinations of τ and D are used to illustrate the theory for competition and oscillatory instabilities. The results are presented using plots of the amplitude of each spike $u_{mn} \equiv u(x_n, t)$ versus time. For certain oscillatory examples, we also plot the quantity b_j^{amp} versus time. In our computations, we limit the time-scale to much less than $\mathcal{O}(\epsilon^{-2})$ so that the spikes remain approximately stationary over the time intervals shown.
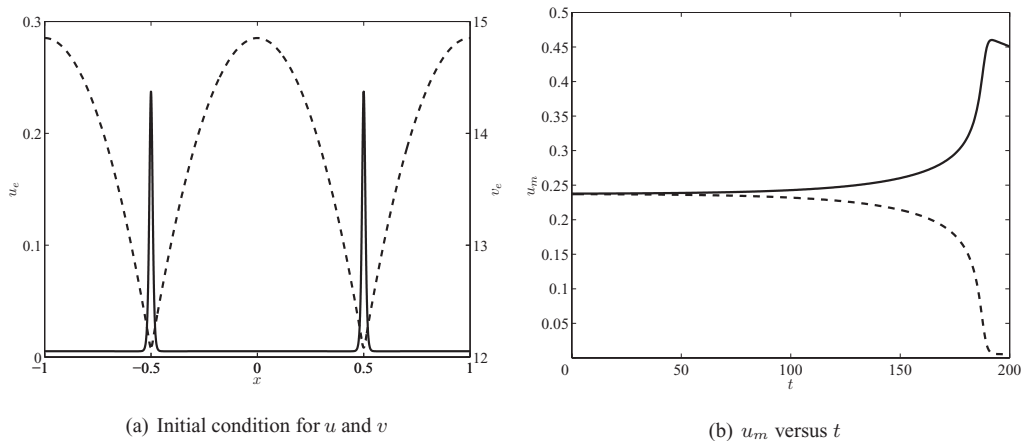
(a) Initial condition for u and v

(b) u_m versus t

FIGURE 7. Experiment 1: The left figure is the initial condition for u (solid curve and left axis) and v (dashed curve and right axis) for $N = 2$ with $\epsilon = 0.005$, $f = 0.5$ and $D = 0.043 > D_{c2} = 0.0417$. The right figure shows the amplitudes of the left (solid curve) and right (dashed curve) spikes for $\tau = 0.01$ versus time. The right spike annihilates as time increases.

Experiment 1 In this experiment we consider competition and oscillatory instabilities of a two-spike equilibrium with $f = 0.5$. We begin with an example of competition instability. For $\epsilon = 0.005$ and $D = 0.043$, in Figure 7(a) we plot the initial conditions for u and v on the left and right axes, respectively. Note the non-zero background of u. Using the results depicted in Figure 2(a), we calculate that $\tau_0(D) = 0.165$, while using (2.45) we calculate $D_{c2} = 0.0417$. For $\tau = 0.01 < \tau_0(D)$ and $D > D_{c2}$, we expect a competition instability in which one spike is annihilated with no oscillation in the amplitudes. In Figure 7(b), we plot the amplitudes u_{m0} and u_{m1} of the two spikes as a function of time. As suggested by the eigenvector v_1 in (2.32c), one spike annihilates as time increases. Note that the spike amplitude decays approximately to the value of the non-zero background state.

We now illustrate oscillatory phenomena. In Figure 8(a), we plot the spike amplitudes when $D = 0.03 < D_{c2}$ and $\tau = 0.17 < \tau_0(D) = \tau_{00} = 0.183$. As expected, no spike annihilations occur while initial oscillations decay. While the equilibrium is stable to large eigenvalues for this combination of D and τ, we calculate from (2.47) that $D > D_2^* = 0.021$. Thus, we expect to observe a drift-type instability when $t = \mathcal{O}(\epsilon^{-2})$. Next, for the same value of D, we set $\tau = 0.191 > \tau_0(D)$ so that the synchronous mode undergoes a Hopf bifurcation. The spike amplitudes are plotted in Figure 8(b). As expected, the spike amplitudes synchronize quickly and oscillate with growing amplitude in time. The eventual annihilation of the spikes suggests that the Hopf bifurcation is subcritical for these parameter values.

In the next example, we take $\epsilon = 0.001$ and $D = 0.006$. In Figure 2(b) we see that for this value of D, the asynchronous oscillatory mode is unstable if $\tau > \tau_0(D) = \tau_{01} = 1.065$, while the synchronous mode is stable if $\tau < \tau_{00} = 1.083$. In Figure 9(a), we plot the spike amplitudes when $\tau = 1.04$ during the initial growth of the oscillations. Note the clear contrast between Figures 9(a) and 8(b), where the spikes oscillate out of phase in the former and in phase in the latter. In Figure 9(b), we show what appears to be regular
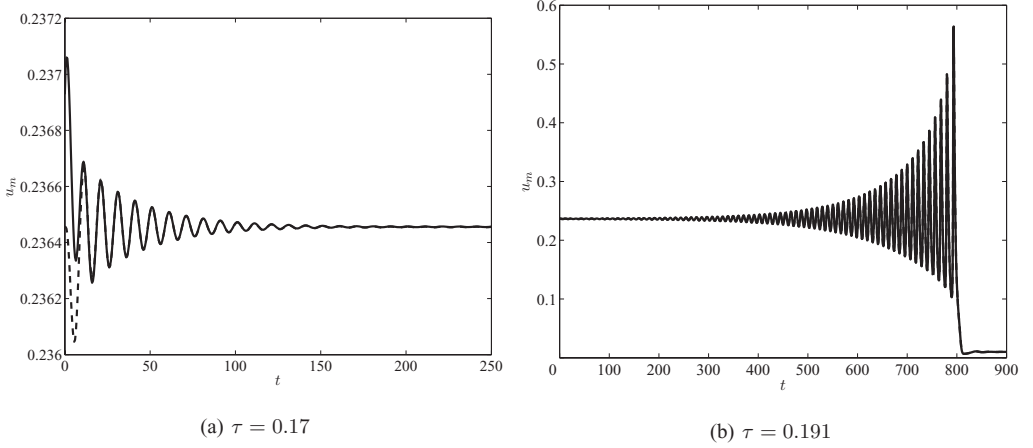
(a) $\tau = 0.17$

(b) $\tau = 0.191$

FIGURE 8. Experiment 1: The left figure is a plot of spike amplitudes for $N = 2$, $\epsilon = 0.005$, $f = 0.5$, $D = 0.03$ and $\tau = 0.17$. The critical value of τ is $\tau_0(D) = 0.183$. The solid curve is u_{m0} and the dashed curve is u_{m1}. In the right figure, we make a similar plot with $\tau = 0.191 > \tau_0(D)$.
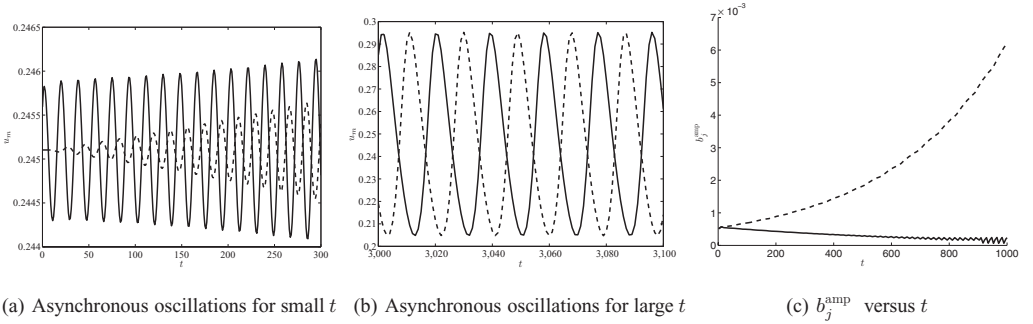

(a) Asynchronous oscillations for small t (b) Asynchronous oscillations for large t (c) b_j^{amp} versus t

FIGURE 9. Experiment 1: In the left figure, we plot spike amplitudes for the initial growth of asynchronous oscillations. In the centre figure, we show the large time behaviour of what appears to be regular asynchronous oscillations. The solid (dashed) curve is u_{m0} (u_{m1}). In the right figure, we plot the initial growth and decay of b_1^{amp} (dashed curve) and b_0^{amp} (solid curve). The parameters are $N = 2$, $\epsilon = 0.001$, $f = 0.6$, $D = 0.006$ and $\tau = 1.04$. The threshold value is $\tau_0(D) = \tau_{01} = 1.065$, and corresponds to asynchronous oscillations.

asynchronous oscillations, suggesting that the Hopf bifurcation may be supercritical for the parameters used. In Figure 9(c) we plot the initial growth of b_1^{amp} and the initial decay of b_0^{amp}, consistent with predictions from analysis. Both modes are present, with the $j = 1$ mode being dominant. We remark that while the numerical threshold in τ is not equal to the theoretical value, we have observed in numerous experiments that agreement with analysis improves as ϵ is decreased.

Experiment 2 In this experiment, we consider instabilities of a three-spike solution with $f = 0.6$. We first consider a competition instability. In Figure 10(a), we plot the initial conditions for u and v for $\epsilon = 0.005$ and $D = 0.017 > D_{c3} = 0.0148$. The initial perturbation, according to v_2 in (2.32c), increases the amplitude of the first and third
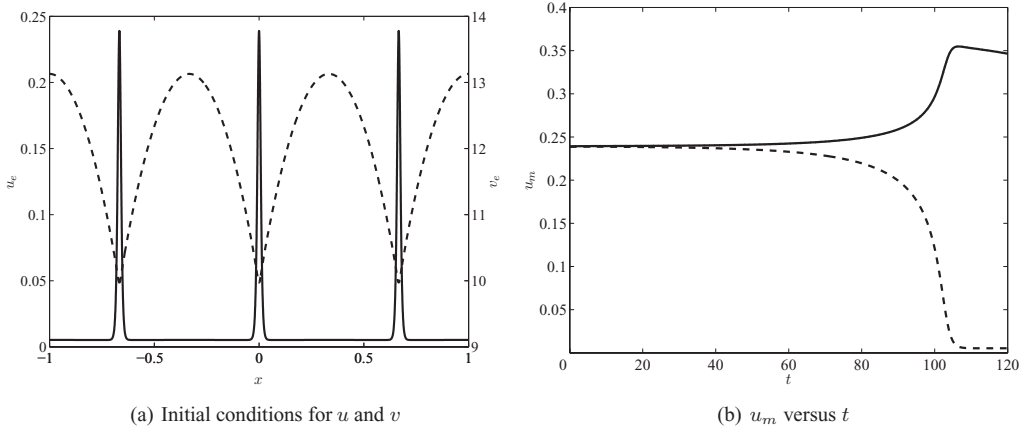
(a) Initial conditions for u and v

(b) u_m versus t

FIGURE 10. Experiment 2: The left figure is the initial condition for u (solid curve and left axis) and v (dashed curve and right axis) for $N = 3$ with $\epsilon = 0.005$, $f = 0.6$ and $D = 0.017 > D_{c3} = 0.0148$. In the right figure, we plot u_{m0} and u_{m2} (solid curve) and u_{m1} (dashed curve) versus time with $\tau = 0.01$. The second spike annihilates as time increases.

spikes while decreasing that of the middle spike. For $\tau = 0.01 < \tau_0(D) = \tau_{00} = 0.28$, we plot the spike amplitudes versus time in Figure 10(b), observing that the middle spike annihilates while the other two spikes increase in amplitude. This increase in amplitude, also observed in Figure 7(b) of Experiment 1, is expected because the common spike amplitude increases when the number of spikes decreases (see (2.8) and (2.15a)). For a perturbation in the $-v_2$ direction we observe the annihilation of the first and third spikes (not shown).

To illustrate oscillatory behaviour, we take $\epsilon = 0.005$ and $D = 0.009$, so that all real eigenvalues lie in the left half-plane if τ is small enough. Using Figure 3(a), we calculate $\tau_0(D) = \tau_{00} = 0.3994$. In Figure 11(a), we set $\tau = 0.37 < \tau_0(D)$, so that oscillations decay in time. For stability also to small eigenvalues, however, we require $D < D_3^* = 0.011$. In Figure 11(b), we set $\tau = 0.42$, so that the spike amplitudes quickly synchronize and the subsequent oscillations grow in time. As in Experiment 1, we observe the annihilation of the spikes, suggesting that the Hopf bifurcation is subcritical.

We next decrease D to $D = 0.0034$ so that, as suggested by Figure 3(b), asynchronous oscillations are the dominant instability. We calculate that $\tau_0(D) = \tau_{02} = 1.518$, $\tau_{01} = 1.544$ and $\tau_{00} = 1.557$. In Figures 12(a) and (b) we plot, respectively, the transient and large time behaviour of the spike amplitudes for $\epsilon = 0.001$ and $\tau = 1.51$. In clear contrast to Figure 11(b), the spike amplitudes oscillate out of phase for both small and large time. In Figure 12(b), as the form of the eigenvector v_2 in (2.32c) suggests, the first and third spikes oscillate approximately in phase with each other, while out of phase with the second spike. For large time, the oscillations occur within an envelope that oscillates slowly in time relative to the oscillations of the spike amplitudes. In Figure 12(c), we plot the initial growth and decay of b_j^{amp} for all three modes. Consistent with the results depicted in Figure 3(b), the $j = 2$ mode grows while the other two modes decay. For large time, all modes are present with the dominant mode being $j = 2$.
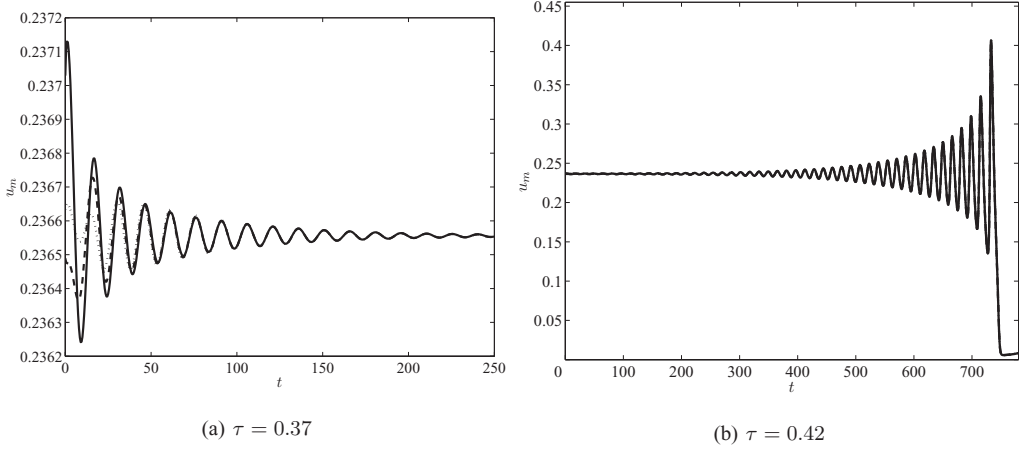
(a) $\tau = 0.37$

(b) $\tau = 0.42$

FIGURE 11. Experiment 2: In the left figure, we plot u_{m0} (solid curve), u_{m1} (dashed curve) and u_{m2} (dotted curve) for $N = 3$, $\epsilon = 0.005$, $f = 0.6$, $D = 0.009$ and $\tau = 0.37$. The right figure is similar except that τ is increased to $\tau = 0.42$. The critical value of τ is $\tau_0(D) = 0.3994$.

(a) Asynchronous oscillations for small t (b) Asynchronous oscillations for large t

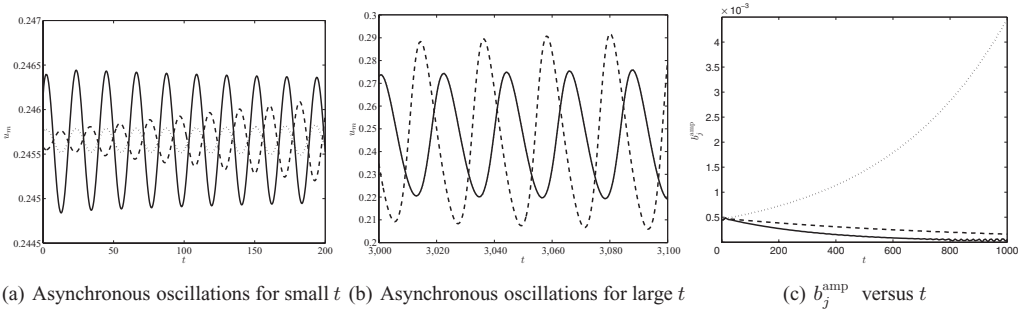(c) b_j^{amp} versus t

FIGURE 12. Experiment 2: In the left and centre figures, we plot, respectively, the transient and large time asynchronous oscillations of u_{m0} (solid curve), u_{m1} (dashed curve) and u_{m2} (dotted curve). The first and third spikes oscillate almost in phase for large time. In the right figure, we plot the initial growth and decay of b_j^{amp} for $j = 0$ (solid curve), $j = 1$ (dashed curve) and $j = 2$ (dotted curve). The parameters are $N = 3$, $\epsilon = 0.001$, $f = 0.6$, $D = 0.0034$ and $\tau = 1.51$. The threshold value is $\tau_0(D) = \tau_{02} = 1.518$.

Experiment 3 In this experiment, we illustrate instabilities of a four-spike equilibrium with $f = 0.6$. In Figure 13(a), we plot the initial conditions for u and v with $\epsilon = 0.005$ and $D = 0.0057$. We calculate from (2.45) that $D_{c4} = 0.0055 < D$. With $\tau = 0.01 < \tau_0(D) = 0.2344$, we expect an annihilation of one or more spikes without oscillatory behaviour. The form of v_3 in (2.32c) suggests that the second spike is the first to annihilate while the fourth spike decays in amplitude as the other two spikes grow. Once the first annihilation occurs, the resulting three-spike pattern is no longer in equilibrium and thus evolves according to the dynamics derived in [27], and any subsequent annihilations should they occur, are beyond the scope of this analysis. In Figure 13(b), we plot the spike amplitudes up to the time of the annihilation of the second spike.
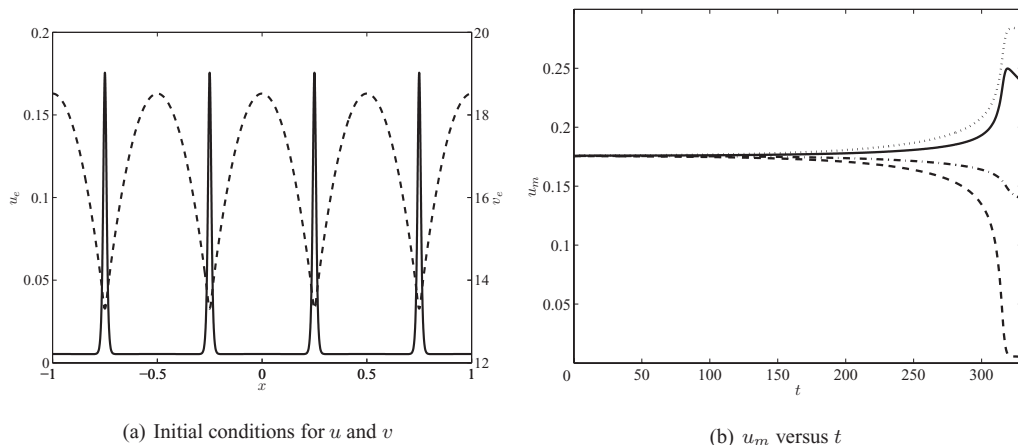
(a) Initial conditions for u and v

(b) u_m versus t

FIGURE 13. Experiment 3: The left figure is the initial condition for u (solid curve and left axis) and v (dashed curve and right axis) for $N = 4$ with $\epsilon = 0.005$, $f = 0.6$ and $D = 0.0057 > D_{c4} = 0.0055$. In the right figure, we plot u_{m0} (solid curve), u_{m1} (dashed curve), u_{m2} (dotted curve) and u_{m3} (dash-dotted) curve versus time with $\tau = 0.01$. The second spike annihilates as time increases. All complex eigenvalues are in the stable left half-plane.
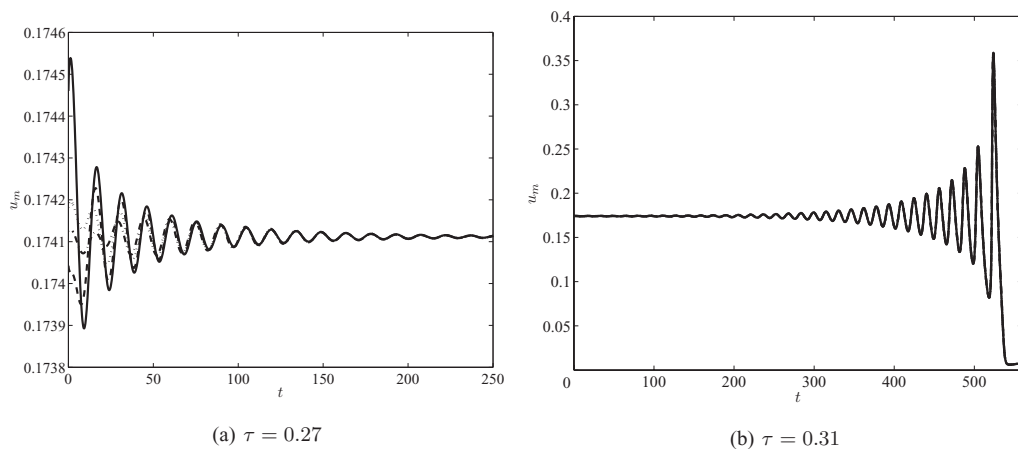

(a) $\tau = 0.27$

(b) $\tau = 0.31$

FIGURE 14. Experiment 3: In the left figure, we plot u_{m0} (solid curve), u_{m1} (dashed curve) and u_{m2} (dotted curve) and u_{m3} (dash-dotted curve) for $N = 4$, $\epsilon = 0.005$, $f = 0.6$, $D = 0.004$ and $\tau = 0.27$. The right figure is similar except $\tau = 0.31$. The critical value of τ is $\tau_0(D) \approx 0.287$.

To show oscillatory phenomena, we take $\epsilon = 0.005$ and $D = 0.004$. Using the data from Figure 4(a), we calculate $\tau_0(D) = \tau_{00} = 0.287$. In Figure 14(a), we plot the spike amplitudes for $\tau = 0.27$ so that the equilibrium solution is stable to large eigenvalues. Here we require $D < D_4^* = 0.00469$ for the equilibrium also to be stable to small eigenvalues. In Figure 14(b), we plot the spike amplitudes for $\tau = 0.31$ so that synchronous oscillations grow in time until all spikes annihilate. As in Experiment 2, we observe oscillatory behaviour subsequent to annihilation.
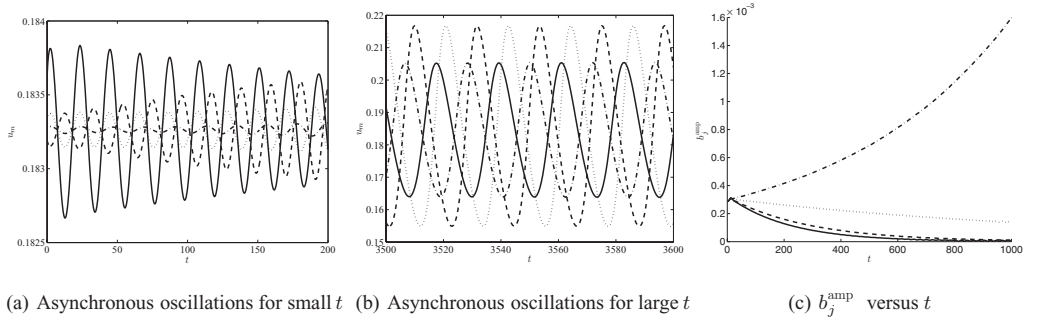
(a) Asynchronous oscillations for small t (b) Asynchronous oscillations for large t (c) b_j^{amp} versus t

FIGURE 15. Experiment 3: In the left and centre figures, we plot, respectively, the transient and large time asynchronous oscillations of u_{m0} (solid curve), u_{m1} (dashed curve), u_{m2} (dotted curve) and u_{m3} (dash-dotted curve). For large time, the first and fourth spikes oscillate approximately π radians out of phase, as do the second and third spikes. In the right figure, we show initial growth and decay of b_j^{amp} for $j = 0$ (solid curve), $j = 1$ (dashed curve), $j = 2$ (dotted curve) and $j = 3$ (dash-dotted curve). The parameters are $N = 4$, $\epsilon = 0.001$, $f = 0.6$, $D = 0.0015$ and $\tau = 1.06$. The critical value of τ is $\tau_0(D) = \tau_{03} = 1.084$.

Lastly, we illustrate asynchronous oscillations with $\epsilon = 0.001$ and $D = 0.0015$. According to the data in Figure 4(b), we calculate that $\tau_0(D) = \tau_{03} = 1.084$, $\tau_{02} = 1.098$, $\tau_{01} = 1.112$ and $\tau_{00} = 1.118$. Taking $\tau = 1.06$, we plot the initial growth of asynchronous oscillations in Figure 15(a). The form of v_3 suggests that the first and fourth spikes oscillate π radians out of phase as should the second and third spikes, while no spikes oscillate in phase. This is shown to be approximately the case for large time in Figure 15(b). The initial growth and decay of the quantities b_j^{amp}, shown in Figure 15(c), demonstrate the reverse ordering principle of the Hopf bifurcation thresholds predicted by the theory. For large time, all modes are present, with the $j = 3$ mode being dominant.

3 Stability of two-spike quasi-equilibria with prescribed boundary flux

In this section, we analyse dynamically triggered instabilities of two-spike quasi-equilibrium solutions to (1.5). In contrast to the equilibrium case studied in Section 2, for which the initial pattern was either stable or unstable depending on the 'tuning' of the model parameters, dynamically triggered instabilities occur when a spike pattern, which is initially stable, eventually undergoes an $\mathcal{O}(1)$ time-scale instability that is triggered by the slow evolution of the spikes. To study this phenomenon, we first construct a two-spike quasi-equilibrium solution and derive an equation of motion for the $\mathcal{O}(\epsilon^2)$ slow dynamics of the spike locations. For the special case of a symmetric two-spike quasi-equilibrium solution, we then derive an NLEP, which depends on the spike locations, that governs the stability of this solution. From an analysis of the NLEP we derive criteria for which a stable quasi-equilibrium solution may become unstable as a result of slow dynamics. We then present numerical examples illustrating the theory. Since general N-spike quasi-equilibria and their slow dynamics have been studied in [27] for the original scaling of the Brusselator model, we omit much of the detail in the analysis of the quasi-equilibrium solution and its slow dynamics.

3.1 Construction and slow dynamics of the two-spike quasi-equilibrium solution

We seek a two-spike quasi-equilibrium solution to (1.5) with spikes centred at x_1 and x_0 with $x_1 > x_0$. As in Section 2.1, in each inner region the leading-order solution for v is $v \sim v_{qej}$ for $j = 0, 1$. Then, as in Section 2.1, we solve (1.5a) for u in the inner region of the jth spike to get

$$u \sim \frac{1}{f v_{qej}} w(y_j), \quad y_j = \epsilon^{-1}(x - x_j), \quad \text{for } j = 0, 1,$$

where $w(y)$ is the solution to (2.2). In the outer region $u \sim \epsilon E + \mathcal{O}(\epsilon^2)$. Then, upon representing the terms involving u in (1.5b) as delta masses, we proceed as in Section 2.1 and use (2.3) to obtain the outer equation for v, which is

$$Dv_{xx} + E - \frac{6}{f^2}(1 - f) \sum_{j=0}^{1} \frac{\delta(x - x_j)}{v_{qej}} = 0, \quad -1 < x < 1; \quad v_x(\pm 1) = \pm 1. \tag{3.1}$$

Upon integrating (3.1) over the interval $-1 < x < 1$ and applying the boundary conditions, we calculate that

$$\sum_{j=0}^{1} \frac{1}{v_{qej}} = \frac{(E + D)}{3} \frac{f^2}{1 - f} > 0. \tag{3.2}$$

For the special case of a symmetric two-spike quasi-equilibrium where $x_1 = -x_0 = \alpha$, then $v_{qe0} = v_{qe1} \equiv v_{cqe}$, where v_{cqe} is given by

$$v_{cqe} = \frac{6}{f^2(D + E)}(1 - f) > 0. \tag{3.3}$$

Note that due to the presence of boundary flux, the spike amplitudes depend on the inhibitor diffusion coefficient.

Next, we let $v = x^2/2 + v(x)$ and solve for $v(x)$ in terms of G, as defined in (2.13). Then we impose the matching condition that $v(x_j) = v_{qej}$ for $j = 0, 1$. In this way, we obtain the following result for the quasi-equilibrium solution:

Principal Result 3.1 *Let $\epsilon \to 0$ in (1.5) and consider a two-spike quasi-equilibrium solution with spikes centred at x_1 and x_0 with $x_1 > x_0$. Then the leading-order composite solution for u is*

$$u_{qe} \sim \epsilon E + \frac{1}{f v_{qe0}} w\left[\epsilon^{-1}(x - x_0)\right] + \frac{1}{f v_{qe1}} w\left[\epsilon^{-1}(x - x_1)\right], \tag{3.4a}$$

while the leading-order outer solution v_{qe} for v is given by

$$v_{qe} \sim \bar{v} + \frac{x^2}{2} + \frac{6}{f^2}(1 - f) \sum_{j=0}^{1} \frac{1}{v_{qej}} G(x; x_j), \tag{3.4b}$$

where G is the Neumann Green's function defined in (2.13). Here v_{qe0}, v_{qe1} and $\bar{v}$ satisfy the coupled system consisting of (3.2) and

$$v_{qe0} = \bar{v} + \frac{x_0^2}{2} + \frac{6}{f^2}(1-f)\left(\frac{G(x_0;x_0)}{v_{qe0}} + \frac{G(x_0;x_1)}{v_{qe1}}\right), \tag{3.5a}$$

$$v_{qe1} = \bar{v} + \frac{x_1^2}{2} + \frac{6}{f^2}(1-f)\left(\frac{G(x_1;x_0)}{v_{qe0}} + \frac{G(x_1;x_1)}{v_{qe1}}\right). \tag{3.5b}$$

By subtracting the two equations in (3.5), and then using (2.13) for G, we obtain that v_{qe0} and v_{qe1} satisfy

$$v_{qe1} - v_{qe0} = a - b\left(\frac{1}{v_{qe1}} - \frac{1}{v_{qe0}}\right), \qquad \frac{1}{v_{qe0}} + \frac{1}{v_{qe1}} = c, \tag{3.6a}$$

where we have defined a, b and c, by

$$a \equiv -\frac{E}{2D}(x_1^2 - x_0^2), \qquad b \equiv \zeta_0(x_1 - x_0) > 0, \qquad c \equiv \frac{1}{\zeta_0}\left(1 + \frac{E}{D}\right) > 0,$$

$$\zeta_0 \equiv \frac{3}{Df^2}(1-f) > 0. \tag{3.6b}$$

By eliminating v_{qe0} in (3.6a), we readily derive that

$$v_{qe0} = \frac{\xi}{c(\xi - 1)}, \qquad v_{qe1} = \frac{\xi}{c}, \tag{3.7a}$$

where ξ is a root of the cubic

$$\mathcal{K}(\xi) \equiv (\xi - 2)(\xi^2 - bc^2\xi + bc^2) + ac\xi(1 - \xi) = 0 \tag{3.7b}$$

on the interval $\xi > 1$.

In discussing the solvability of (3.7) we will consider two cases: Case 1 where $x_1 = -x_0$, and Case 2 where $x_1 \neq x_0$. For Case I, suppose that the initial data is such that $x_1 = -x_0$ at time $t = 0$. Since $a = 0$, we obtain that (3.7b) has a unique root $\xi = 2$ when $c < 2/\sqrt{b}$, and it has three roots $\xi = 2$ and $\xi = \xi_\pm > 1$ when $c > 2/\sqrt{b}$, where $\xi_\pm$ is defined by

$$\xi_\pm = \frac{bc^2}{2}\left[1 \pm \sqrt{1 - \frac{4}{bc^2}}\right], \qquad \text{for } c > 2/\sqrt{b}. \tag{3.8}$$

Therefore, when $x_1 = -x_0$, we have a symmetric two-spike quasi-equilibrium solution with $v_{qe0} = v_{qe1} = 2/c$, and two asymmetric quasi-equilibrium solutions with either $v_{qe0} < v_{qe1}$ or $v_{qe1} < v_{qe0}$ that exist when $c > 2/\sqrt{b}$. These asymmetric quasi-equilibria arise from a pitchfork bifurcation at the critical value $c = 2/\sqrt{b}$.

Remark 1 From an analysis of an NLEP in Section 3.2 (see (3.29)), we will show that the two asymmetric quasi-equilibria for $x_1 = -x_0$ and $c > 2/\sqrt{b}$ are unstable on an $\mathcal{O}(1)$ time-scale for any $\tau \geqslant 0$.

Next, we briefly consider the generic Case II where $x_1 \neq x_0$, so that $a \neq 0$. Then, since $\mathcal{K}(1) = -1 < 0$ and $\mathcal{K} \to +\infty$ as $\xi \to +\infty$, there is always a root to (3.7b) on $\xi > 1$. Therefore, there always exists a two-spike quasi-equilibrium state for any $x_1 > x_0$. By plotting $\mathcal{K}(\xi)$, it readily follows that there is a unique root to $\mathcal{K}(\xi) = 0$ when $|a| \gg 1$. For smaller values of $|a|$ and when $bc^2 > 4$, there can be three quasi-equilibrium states. Since $\mathcal{K}(\xi)$ is a cubic, which therefore has at most two critical points, a sufficient condition for $\mathcal{K}(\xi) = 0$ to have a unique root on $\xi > 1$ is that $\mathcal{K}'(1) < 0$. This yields the inequality $bc^2 - ac < 1$.

Next, we derive the $\mathcal{O}(\epsilon^2)$ slow dynamics of the spike locations. We introduce the slow time variable $\sigma = \epsilon^2 t$ and retain the next terms in the asymptotic series for the inner solutions of u and v near x_j as

$$u = \frac{1}{f v_{qej}} w(y_j) + \epsilon U_{1j}(y_j), \quad v = v_{qej} + \epsilon V_{1j}(y_j); \quad y_j = \epsilon^{-1}\left[x - x_j(\sigma)\right], \quad \sigma = \epsilon^2 t. \quad (3.9)$$

Substituting (3.9) into (1.5), and collecting terms of similar order, we obtain

$$L_0 U_{1j} = -\frac{\dot{x}_j}{f v_{qej}} w' - E - \frac{w^2}{f v_{qej}^2} V_{1j}, \quad -\infty < y_j < \infty, \quad U_{1j}' \to 0 \text{ as } |y_j| \to \infty, \quad (3.10a)$$

$$D V_{1j}'' = -\frac{w}{f v_{qej}} + \frac{w^2}{f^2 v_{qej}}, \quad -\infty < y_j < \infty, \quad V_{1j}' \to v_{qex}(x_j^{\pm}) \text{ as } y_j \to \pm\infty, \quad (3.10b)$$

where $\dot{x}_j \equiv dx_j/d\sigma$ and the operator L_0 is defined in (2.28). The limiting condition in (3.10b) comes from matching the gradients of the inner and outer solutions of v. In (3.10a), L_0 has a one-dimensional kernel with eigenfunction w'. Thus, the right-hand side of (3.10a) must be orthogonal to w'. This solvability condition yields

$$-\frac{\dot{x}_j}{f v_{qej}} \int_{-\infty}^{\infty} (w')^2 \, dy_j - E \int_{-\infty}^{\infty} w' \, dy_j - \frac{1}{f v_{qej}^2} \int_{-\infty}^{\infty} w' w^2 V_{1j} \, dy_j = 0.$$

Since w' is odd and $w'w^2 = (w^3)'/3$, we can integrate by parts and use $w \to 0$ as $|y_j| \to \infty$ to obtain

$$\dot{x}_j \int_{-\infty}^{\infty} (w')^2 \, dy_j = \frac{1}{3 v_{qej}} \int_{-\infty}^{\infty} w^3 V_{1j}' \, dy_j. \quad (3.11)$$

Next, we integrate by parts on the right-hand side of (3.11). Using the facts that $\int_0^{y_j} w^3(s) \, ds$ is odd and that, by (3.10b), V_{1j} is even, we calculate that

$$\dot{x}_j \int_{-\infty}^{\infty} (w')^2 \, dy_j = \frac{1}{6 v_{qej}} \int_{-\infty}^{\infty} w^3 \, dy_j \left[V_{1j}'(\infty) + V_{1j}'(-\infty)\right]. \quad (3.12)$$

Finally, since $\frac{\int_{-\infty}^{\infty} w^3 \, dy_j}{\int_{-\infty}^{\infty} (w')^2 \, dy_j} = 6$, we can apply the limiting conditions for V_{1j} in (3.10b) to reduce (3.12) to

$$\dot{x}_j = \frac{1}{v_{qej}} \left[v_{qex}(x_j^+) + v_{qex}(x_j^-)\right]. \quad (3.13)$$

To calculate the right-hand side of (3.13), we use (3.4b) and (2.13). In this way, we obtain the following ODE–differential algebraic equation (DAE) system characterizing the slow dynamics of x_0 and x_1:

Principal Result 3.2 *Consider the quasi-equilibrium solution* (3.4) *of* (1.5) *with spikes centred at x_1 and x_0 with $-1 < x_0 < x_1 < 1$. Then, for $\epsilon \to 0$, and provided that the quasi-equilibrium profile is stable to $\mathcal{O}(1)$ time-scale instabilities, the spikes drift with speed $\mathcal{O}(\epsilon^2)$ according to the asymptotic ODE–DAE system*

$$\dot{x}_0 \sim \frac{2}{v_{qe0}} \left[x_0 - \zeta_0 \left(\frac{x_0}{v_{qe0}} + \frac{(1+x_0)}{v_{qe1}} \right) \right] , \qquad \dot{x}_1 \sim \frac{2}{v_{qe1}} \left[x_1 + \zeta_0 \left(\frac{(1-x_1)}{v_{qe0}} - \frac{x_1}{v_{qe1}} \right) \right].$$
(3.14)

Here v_{qe0} and v_{qe1}, which depend on x_0 and x_1, are positive solutions of the nonlinear algebraic system (3.6), while ζ_0 is defined in (3.6b).

For the special case of a symmetric two-spike quasi-equilibrium solution with $x_1 = -x_0 \equiv \alpha$ and $v_{qe1} = v_{qe0} = v_{cqe}$, we use (3.3) to simplify (3.14). This leads to the following result:

Principal Result 3.3 *Consider the quasi-equilibrium solution* (3.4) *of* (1.5) *with spikes centred at $x_1 = -x_0 \equiv \alpha$ for $0 < \alpha < 1$, for which the spikes have a common amplitude, i.e. $v_{qe0} = v_{qe1} = v_{cqe}$. Then, for $\epsilon \to 0$, and provided that the quasi-equilibrium profile is stable to $\mathcal{O}(1)$ time-scale instabilities, the spikes drift with speed $\mathcal{O}(\epsilon^2)$ according to the ODE*

$$\frac{d\alpha}{dt} \sim \epsilon^2 \mathscr{H}(\alpha) ; \qquad \mathscr{H}(\alpha) \equiv \frac{1}{v_{cqe}} \left[1 + \frac{E}{D} - \frac{2\alpha E}{D} \right] .$$
(3.15)

Here v_{cqe}, which is independent of the spike locations, is defined in (3.3). The equilibrium locations of the spikes are at $\pm\alpha_e$ where $\mathscr{H}(\alpha_e) = 0$, which yields

$$\alpha_e = \frac{1}{2} + \frac{D}{2E} .$$
(3.16)

Due to the imposed boundary flux, these equilibrium locations are not at the symmetry locations $\pm 1/2$ of the no boundary flux system studied previously in Section 2. From (3.16), we observe that for the equilibrium locations to be inside the domain, we must have $D/E < 1$. Since $\mathscr{H}'(\alpha_e) < 0$, the equilibrium points of the ODE are always stable.

We limit our study to the parameter range where the inequality $D/E < 1$ is satisfied. We note that the symmetric equilibrium is stable under the dynamics (3.15), which was derived under the assumption that $x_0 = -x_1$. That is, the equilibrium (3.16) is stable only to perturbations that preserve this symmetry. For the equilibrium to be stable to any perturbation, including to those that break the symmetry, the parameters D, E and f must satisfy the following condition (cf. [27]):

$$\frac{1-f}{Ef^2} < \frac{1}{24} \frac{E}{D} \left[1 + \frac{D}{E} \right]^3 .$$
(3.17)

The criterion (3.17), as derived in [27], is the condition that must be satisfied for a two-spike symmetric equilibrium solution to be stable to eigenvalues of $\mathcal{O}(\epsilon^2)$.

3.2 Derivation of NLEP

In this section we study the stability of the two-spike quasi-equilibrium solution with respect to large eigenvalues with $\lambda = \mathcal{O}(1)$ as $\epsilon \to 0$. This is done by first deriving the NLEP governing the stability on an $\mathcal{O}(1)$ time-scale of the two-spike quasi-equilibrium solution of Principal Result 3.1 associated with (1.5). Since this NLEP has the same form as in (2.39), differing only in the coefficient of the non-local term, we will only briefly outline its derivation.

We linearize about the quasi-equilibrium solution of (3.4) by writing $u = u_{qe} + e^{\lambda t}\Phi$ and $v = v_{qe} + e^{\lambda t}\Psi$. Substituting this into (1.5), we then follow the same procedure as used in (2.17)–(2.39). In place of the vector NLEP (2.29), we obtain that $\boldsymbol{\Phi} \equiv (\Phi_0, \Phi_1)^t$ satisfies

$$L_0\boldsymbol{\Phi} + \frac{w^2}{fD}\mathcal{V}\mathcal{C}^{-1}\mathcal{G}^{(\mu)}\left[\int_{-\infty}^{\infty}\left(\boldsymbol{\Phi} - \frac{2}{f}w\boldsymbol{\Phi}\right)dy\right] = \lambda\boldsymbol{\Phi}, \tag{3.18}$$

where $\mathcal{C}$, the Neumann Green's matrix $\mathcal{G}^{(\mu)}$ and the diagonal matrix $\mathcal{V}$ are defined by

$$\mathcal{C} = \mathcal{I} + \frac{6}{f^2D}\mathcal{G}^{(\mu)}\mathcal{V}, \quad \mathcal{G}^{(\mu)} \equiv \begin{pmatrix} G^{(\mu)}(x_0;x_0) & G^{(\mu)}(x_0;x_1) \\ G^{(\mu)}(x_1;x_0) & G^{(\mu)}(x_1;x_1) \end{pmatrix}, \quad \mathcal{V} \equiv \begin{pmatrix} 1/v_{qe0}^2 & 0 \\ 0 & 1/v_{qe1}^2 \end{pmatrix}. \tag{3.19}$$

Here $G^{(\mu)}(x;x_j)$ is the Neumann Green's function satisfying (2.23).

To obtain two uncoupled scalar NLEPs, we diagonalize $\mathcal{C}^{-1}$ and $\mathcal{G}^{(\mu)}$ by using the spectral decomposition of $\mathcal{G}^{(\mu)}\mathcal{V}$ given by

$$\mathcal{G}^{(\mu)}\mathcal{V} = \mathcal{S}\Lambda\mathcal{S}^{-1}, \quad \mathcal{C}^{-1}\mathcal{G}^{(\mu)}\mathcal{V} = \mathcal{S}\left[\mathcal{I} + \frac{6}{f^2D}\Lambda\right]^{-1}\Lambda\mathcal{S}^{-1}, \tag{3.20}$$

where Λ is the diagonal matrix of the eigenvalues $\tilde{\kappa}_0$ and $\tilde{\kappa}_1$ of $\mathcal{G}^{(\mu)}\mathcal{V}$. Then, upon substituting (3.20) and $\boldsymbol{\Phi} = \mathcal{V}S\hat{\boldsymbol{\Phi}}$ into (3.18), we obtain in place of (2.34) the two uncoupled NLEPs:

$$L_0\hat{\Phi} + f\tilde{\chi}_j w^2 \left(\frac{\int_{-\infty}^{\infty}\left(\hat{\Phi} - \frac{2}{f}w\hat{\Phi}\right)dy}{\int_{-\infty}^{\infty}w^2\,dy}\right) = \lambda\hat{\Phi}, \quad j = 0,1; \quad \tilde{\chi}_j \equiv \frac{\tilde{\kappa}_j}{\tilde{\kappa}_j + \frac{Df^2}{6}}. \tag{3.21}$$

Finally, by proceeding as in (2.36) and (2.37) to eliminate one of the non-local terms in (3.21), we obtain the following result:

Principal Result 3.4 *For $\epsilon \to 0$, consider the quasi-equilibrium solution (3.4) of (1.5) with spikes centred at x_1 and x_0 with $-1 < x_0 < x_1 < 1$. Then the stability of this solution on*

an $\mathcal{O}(1)$ time-scale is determined by the spectrum of NLEP,

$$L_0\hat{\Phi} - \chi_j w^2 \left(\frac{\int_{-\infty}^{\infty} w\hat{\Phi}\, dy}{\int_{-\infty}^{\infty} w^2\, dy} \right) = \lambda\hat{\Phi}, \tag{3.22}$$

where $\chi_j = \chi_j(\lambda)$ is defined by

$$\chi_j \equiv 2\tilde{\chi}_j \left[\frac{1 + \lambda - f}{1 + \lambda - \tilde{\chi}_j f} \right], \qquad \tilde{\chi}_j = \frac{\tilde{\kappa}_j}{\tilde{\kappa}_j + \frac{Df^2}{6}}, \qquad j = 0, 1. \tag{3.23}$$

Here $\tilde{\kappa}_j$ for $j = 0, 1$, which also depend on λ, are the eigenvalues of the matrix product $\mathscr{G}^{(\mu)}\mathscr{V}$ defined in (3.19).

We now analyse this NLEP to derive an instability threshold for a two-spike quasi-equilibrium solution with arbitrary spike locations $x_1 > x_0$. The analysis in Section 3.3 proves that if $\chi_j(0) < 1$ for either $j = 0, 1$, then the NLEP in (3.22) has a positive real eigenvalue for any $\tau \geqslant 0$. If $\chi_j(0) = 1$, then $\lambda = 0$ is an eigenvalue of (3.22) with eigenfunction $\hat{\Phi} = w$. Furthermore, if $\chi_j(0) > 1$ for $j = 0, 1$, then $\mathrm{Re}(\lambda) < 0$ for τ sufficiently small. Upon using (3.23), we obtain that the condition $\chi_j(0) < 1$ is equivalent to

$$\tilde{\kappa}_j|_{\lambda=0} < \frac{Df^2}{6(1-f)}. \tag{3.24}$$

To calculate the two eigenvalues $\tilde{\kappa}_j$ of $\mathscr{G}^{(\mu)}\mathscr{V}$ for $\lambda = 0$, we expand $\mathscr{G}^{(\mu)}$ as $\mu^2 \to 0$, to obtain that

$$\mathscr{G}^{(\mu)} \sim \frac{1}{2\mu^2} \begin{pmatrix} 1 & 1 \\ 1 & 1 \end{pmatrix} - \begin{pmatrix} G(x_0; x_0) & G(x_0; x_1) \\ G(x_1; x_0) & G(x_1; x_1) \end{pmatrix}, \tag{3.25}$$

where $\mu^2 = \tau\lambda/D$ and $G(x; x_j)$ is the Neumann Green's function of (2.12) with $D = 1$. By using (2.13) for G with $D = 1$, we calculate for $\mu^2 \ll 1$ that

$$\mathscr{G}^{(\mu)}\mathscr{V} \sim \left(\frac{1}{2\mu^2} + \frac{1}{6} \right)\mathscr{A} + \mathscr{D}, \quad \mathscr{A} \equiv \begin{pmatrix} 1/v_{qe0}^2 & 1/v_{qe1}^2 \\ 1/v_{qe0}^2 & 1/v_{qe1}^2 \end{pmatrix},$$

$$\mathscr{D} \equiv \begin{pmatrix} \dfrac{x_0^2}{2v_{qe0}^2} & \dfrac{(x_0^2 + x_1^2)}{4v_{qe1}^2} - \dfrac{(x_1 - x_0)}{2v_{qe1}^2} \\ \dfrac{(x_0^2 + x_1^2)}{4v_{qe0}^2} - \dfrac{(x_1 - x_0)}{2v_{qe0}^2} & \dfrac{x_1^2}{2v_{qe1}^2} \end{pmatrix}. \tag{3.26}$$

To leading order in μ, the eigenvectors v_j and eigenvalues $\tilde{\kappa}_j$ of $\mathscr{G}^{(\mu)}\mathscr{V}$ are the eigenvectors of $\mathscr{A}$. Therefore, for $\mu^2 \ll 1$, we get $v_0 \sim (1, 1)^t$ and $v_1 \sim (v_{qe0}^2, -v_{qe1}^2)^t$. This shows that $\tilde{\kappa}_0 \to +\infty$ as $\lambda \to 0$ so that $\chi_0(0) = 2 > 1$. We conclude that the synchronous mode $v_0 \sim (1, 1)^t$ does not generate any instabilities when $\tau \ll 1$. Alternatively, for the competition mode v_1, we have $\mathscr{A}v_1 = 0$ so that $\tilde{\kappa}_1 = \mathcal{O}(1)$ as $\mu^2 \to 0$. From a routine matrix eigenvalue perturbation calculation we calculate for $\mu^2 = \tau\lambda/D \ll 1$ that

$$\tilde{\kappa}_1 \sim \frac{v_1^t \mathscr{D} v_1}{v_1^t v_1} = \frac{1}{2(v_{qe0}^4 + v_{qe1}^4)} \left[\frac{(x_1^2 - x_0^2)}{2}\left(v_{qe1}^2 - v_{qe0}^2\right) + (x_1 - x_0)\left(v_{qe0}^2 + v_{qe1}^2\right) \right]. \tag{3.27}$$

By combining (3.27) and (3.24), we obtain an instability criterion for the arbitrary two-spike quasi-equilibrium solution of Principal Result 3.1.

Principal Result 3.5 *The two-spike quasi-equilibrium solution of Principal Result 3.1 is unstable on an $\mathcal{O}(1)$ time-scale for any $\tau \geqslant 0$, when*

$$\frac{1}{2(v_{qe0}^4 + v_{qe1}^4)} \left[\frac{(x_1^2 - x_0^2)}{2} \left(v_{qe1}^2 - v_{qe0}^2\right) + (x_1 - x_0)\left(v_{qe0}^2 + v_{qe1}^2\right) \right] < \frac{Df^2}{6(1-f)} = \frac{1}{2\zeta_0}, \quad (3.28)$$

where ζ_0 is defined in (3.6b). Here v_{qe0} and v_{qe1} is any solution to the nonlinear algebraic system (3.6).

We now use (3.28) to prove for the case $x_1 = -x_0$ that the two asymmetric quasi-equilibrium solutions obtained in (3.8) for $c > 2/\sqrt{b}$ are unstable on an $\mathcal{O}(1)$ time-scale. This will establish Remark 1 of Section 3.1. For $x_1 = -x_0$, (3.28) implies that we have instability when

$$\frac{(v_{qe0}^2 + v_{qe1}^2)}{(v_{qe0}^4 + v_{qe1}^4)} < \frac{1}{2\zeta_0 x_1} = \frac{1}{b}. \quad (3.29)$$

However, since $v_{qe0} = b/v_{qe1}$ when $a = 0$ in (3.6a), this instability inequality holds when $v_{qe1}^2 + b^4/v_{qe1}^4 > b(v_{qe1}^2 + b^2/v_{qe1}^2)$. Upon setting $y = v_{qe1}/\sqrt{b}$, this inequality reduces to showing that $y^4 + 1/y^4 > y^2 + 1/y^2$ for all $0 < y < \infty$ with $y \neq 1$. Defining z by $z = y^2 + 1/y^2$, for which $z > 2$ for any $y \neq 1$, the inequality $y^4 + 1/y^4 > y^2 + 1/y^2$ is equivalent to showing the obvious result that $z^2 - z - 2 > 0$ when $z > 2$. This establishes Remark 1.

The instability criterion (3.28) can be used together with a numerical simulation of the DAE system in Principal Result 3.2 to characterize when the slow spike motion, as predicted by (3.14), ceases to be valid due to the triggering of an $\mathcal{O}(1)$ time-scale instability. Rather than investigating this problem numerically, for the remainder of this section we will restrict the analysis to the simpler case of symmetric two-spike quasi-equilibria where $x_1 = -x_0$ and $v_{qe0} = v_{qe1} \equiv v_{cqe}$, which is analytically more tractable.

For such a symmetric two-spike quasi-equilibrium solution, then $\mathcal{V}$ is a multiple of a diagonal matrix and $\mathcal{G}^{(\mu)}$ is a symmetric matrix with constant row sum. Thus, the eigenvectors of $\mathcal{G}^{(\mu)}$ are $(1,1)^t$ and $(1,-1)^t$. To calculate the eigenvalues of $\mathcal{G}^{(\mu)}$ in this case, we proceed as in [25] and write $\mathcal{G}^{(\mu)} = \mathcal{B}^{-1}/\mu$, where $\mathcal{B}$ is given in Section 2 of [25] as

$$\mathcal{B}_\alpha \equiv \begin{pmatrix} d_\alpha & f_\alpha \\ f_\alpha & d_\alpha \end{pmatrix}; \qquad d_\alpha \equiv \coth(2\mu\alpha) + \tanh\left[\mu(1-\alpha)\right], \quad f_\alpha \equiv -\operatorname{csch}(2\mu\alpha). \quad (3.30)$$

Here $\mu^2 = \tau\lambda/D$ is defined in (2.21). The eigenvalues σ_0 and σ_1 of $\mathcal{B}_\alpha$ and the corresponding eigenvectors v_0 and v_1 are

$$\begin{aligned} \sigma_0 &= \tanh(\mu\alpha) + \tanh\left[\mu(1-\alpha)\right]; & v_0 &= (1,1)^t, \\ \sigma_1 &= \coth(\mu\alpha) + \tanh\left[\mu(1-\alpha)\right]; & v_1 &= (1,-1)^t. \end{aligned} \quad (3.31)$$

The eigenvalues $\tilde{\kappa}_j$ of matrix $\mathcal{G}^{(\mu)}\mathcal{V}$ are then given by $\tilde{\kappa}_j = 1/(\mu v_{cqe}^2 \sigma_j)$, for $j = 0, 1$.

In terms of σ_j, the NLEP in (3.22) corresponding to a symmetric two-spike quasi-equilibrium solution reduces to the following:

Principal Result 3.6 *Let $\epsilon \to 0$ and consider the two-spike symmetric quasi-equilibrium solution with $x_1 = -x_0$ and $v_{qe1} = v_{qe0} \equiv v_{cqe}$, as given in (3.4). The stability of this quasi-equilibrium solution on an $\mathcal{O}(1)$ time-scale is determined by the spectrum of NLEP in (3.22), where χ_j is defined by*

$$\chi_j = \frac{2}{1 + \mu\sigma_j/\beta} \left[1 + \frac{f\mu\sigma_j}{f\beta - (1+\lambda)(\beta + \mu\sigma_j)} \right], \quad j = 0, 1; \quad \beta \equiv \frac{(D+E)^2 f^2}{6D(1-f)^2}. \quad (3.32)$$

The discrete eigenvalues of (2.39a) are the roots of the transcendental equations $g_j(\lambda) = 0$, where

$$g_j(\lambda) \equiv C_j(\lambda) - F(\lambda), \quad C_j(\lambda) \equiv \frac{1}{\chi_j(\lambda)}. \quad (3.33)$$

Here $F(\lambda)$ is defined in (2.40), and $C_j(\lambda)$ is given by

$$C_j(\lambda) = \frac{1}{2} \left[1 + \xi_j + \frac{f\xi_j}{1 + \lambda - f} \right], \quad \xi_j \equiv \frac{\mu\sigma_j}{\beta}. \quad (3.34)$$

3.3 Dynamically triggered competition instabilities; symmetric quasi-equilibria

We now calculate a value α_c such that the symmetric quasi-equilibrium solution with spikes at $x_1 = -x_0 \equiv \alpha$ is unstable to a competition instability when $\alpha < \alpha_c$ for $\tau = 0$. Thus, a competition instability is dynamically triggered if the condition $\alpha_e < \alpha_c < \alpha(0) < 1$ holds. For then, $\alpha(t)$ will dip below α_c on its approach to its equilibrium state α_e. In Section 3.4, we calculate the Hopf bifurcation thresholds as a function of α, analogous to those calculated in Section 2.4, and we find that dynamically triggered oscillatory instabilities can also occur.

To determine α_c, we look for roots to (3.33) on the positive real axis. The analysis here is similar to that in Section 2.3. We first consider the case where $\tau = 0$. To find real positive roots of $g_j(\lambda)$ as $\tau \to 0$, we let $\mu \to 0$ in (3.31) to obtain $\xi_0 \to 0$ and $\xi_1 \to (\alpha\beta)^{-1}$ as $\tau \to 0$. Then, from (3.33) and (3.34), we have $C_0 = 1/2 < 1$ so that the synchronous mode $(1, 1)^t$ is always stable when $\tau = 0$. Here we have used the properties (2.41) for $F(\lambda)$. Alternatively, when $\tau = 0$, we have from (3.34) that

$$C_1(\lambda) = \frac{1}{2} \left[1 + \xi_1 + \frac{f\xi_1}{1 + \lambda - f} \right], \quad \xi_1 \equiv 1/(\alpha\beta). \quad (3.35)$$

Since $C_1(\lambda)$ is a positive decreasing function of λ while $F(\lambda)$ has the properties in (2.41), g_1 has a unique positive real root if $C_1(0) > 1$ and no roots if $C_1(0) < 1$. A winding number argument similar to that used in Section 2.3 can be used to show that no other roots exist in the right half-plane. This leads to the following stability criteria:

Principal Result 3.7 *For $\tau = 0$, consider the quasi-equilibrium solution (3.4) to (1.5) with spikes centred at $x = \pm\alpha$ for $0 < \alpha < 1$, and where the spikes have a common amplitude. The solution is stable on an $\mathcal{O}(1)$ time-scale if and only if*

$$\alpha > \alpha_c; \quad \alpha_c \equiv \frac{6D(1-f)}{(D+E)^2 f^2}. \tag{3.36}$$

If the inequality in (3.36) is reversed, the quasi-equilibrium profile is unstable to one real positive eigenvalue corresponding to the $(1, -1)^t$ mode, which conserves the sum of the amplitudes of the spikes. Note that if $D \ll 1$ but $D \gg \mathcal{O}(\epsilon^2)$, we have $\alpha_c \sim 6D(1-f)/(E^2 f^2) \ll 1$ so that the region of stability spans almost the entire range $0 < \alpha < 1$. Also, from (3.36), we see that $\alpha_c \sim \mathcal{O}(D^{-1})$ as $D \to \infty$. We remark that the condition $\alpha > \alpha_c$ is equivalent to the condition $c > 2/\sqrt{b}$ in the analysis of the quasi-equilibria in (3.8).

As discussed earlier, a symmetric two-spike quasi-equilibrium solution can undergo a dynamic competition instability whenever $\alpha_e < \alpha_c < 1$. By using the expression for α_e in (3.16), we have the following result:

Principal Result 3.8 *The quasi-equilibrium solution in (3.4) with a rightmost initial spike location $\alpha(0)$ satisfying $\alpha(0) > \alpha_c$ will undergo a dynamic competition instability at some time $t > 0$ when $\alpha_e < \alpha_c < 1$. These inequalities hold when*

$$\frac{1}{12}\frac{E}{D}\left[1 + \frac{D}{E}\right]^3 < \frac{1-f}{Ef^2} < \frac{1}{6}\frac{E}{D}\left[1 + \frac{D}{E}\right]^2. \tag{3.37}$$

The region described by (3.37) is plotted in Figure 16. Above the dotted curve a competition instability occurs starting at $t = 0$ for any $\alpha(0)$, while below the solid curve the two-spike quasi-equilibrium solution is stable to the large eigenvalues and there is no competition instability for any $\alpha(0)$ with $\alpha(0) > \alpha_e$.

By comparing the lower bound of (3.37) with (3.17), we conclude that for $\tau = 0$ the two-spike equilibrium solution is stable if and only if it is stable to the small eigenvalues in the limit $\tau \to 0$. The result is written as follows:

Principal Result 3.9 *The symmetric two-spike equilibrium solution in (3.4) with $\alpha = \alpha_e$ is stable with respect to the large eigenvalues but unstable with respect to the small eigenvalues when*

$$\frac{1}{24}\frac{E}{D}\left[1 + \frac{D}{E}\right]^3 < \frac{1-f}{Ef^2} < \frac{1}{12}\frac{E}{D}\left[1 + \frac{D}{E}\right]^3. \tag{3.38}$$

It is stable with respect to the small eigenvalues when (3.17) holds.

For the case $\tau > 0$, it is difficult, owing to the non-monotonicity of the curves $C_j(\lambda)$, to obtain explicit results that count the number of positive real eigenvalues in the right half-plane. However, the following (less precise) results are readily proved.
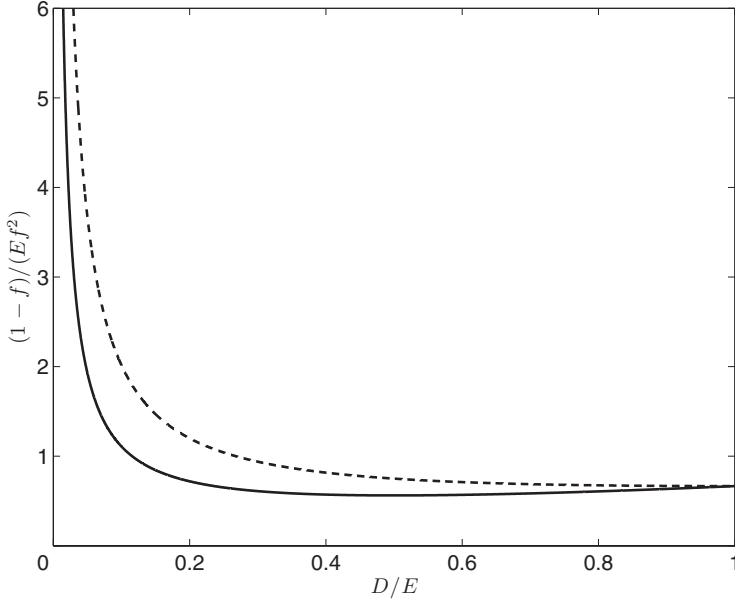
FIGURE 16. The region between the two curves is the parameter space in which a dynamic competition instability is possible for a two-spike pattern with initial state $\alpha(0)$ with $\alpha_e < \alpha(0) < 1$. The horizontal axis is on the range $0 < D/E < 1$ for which a two-spike equilibrium solution exists.

Principal Result 3.10 *Suppose that $\tau \geqslant 0$ and that $0 < \alpha < \alpha_c$. Then the NLEP in Principal Result 3.3 admits at least one real positive eigenvalue. Hence, the quasi-equilibrium pattern is unstable. Alternatively, suppose that $\alpha_c < \alpha < 1$. Then, for $\tau > 0$ sufficiently large, the NLEP in Principal Result 3.3 admits four real positive eigenvalues.*

To prove the first statement, we note that $C_1(0) > 1$ when $\alpha < \alpha_c$. Therefore, the curves $C_1(\lambda)$ and $F(\lambda)$ must have at least one intersection in $\lambda > 0$ when $\tau \geqslant 0$. To prove the second statement we note that $C_j(0) < 1$ when $\alpha > \alpha_c$ for $j = 0, 1$ and that $C_j(\lambda) = \mathcal{O}\left(\sqrt{\tau\lambda}\right)$ for $\lambda > 0$ when $\tau \gg 1$. It follows from the concavity of $C_j(\lambda)$ in the large τ limit and the convexity of $F(\lambda)$ (see properties (2.41)) that for both $j = 0$ and $j = 1$, there are two intersection points of $C_j(\lambda) = F(\lambda)$ on $0 < \lambda < 5/4$.

3.4 Dynamically triggered oscillatory instabilities; symmetric quasi-equilibria

For the parameter range $\alpha_c < \alpha < 1$, we calculate the threshold τ_0 for which the NLEP has a complex conjugate pair of eigenvalues on the imaginary axis. More specifically, we calculate the values $\tau = \tau_{0j}(\alpha)$ such that $g_j = 0$ has a pair of complex conjugate solutions $\lambda = \pm i\lambda_{Ij}^0(\alpha)$ on the imaginary axis. The quantity

$$\tau_0(\alpha) = \min(\tau_{00}, \tau_{01}) \tag{3.39}$$

is then defined to be the Hopf instability threshold. As in Section 2.4, either the $j = 0$ mode, which corresponds to synchronous oscillations, or the $j = 1$ mode, which corresponds
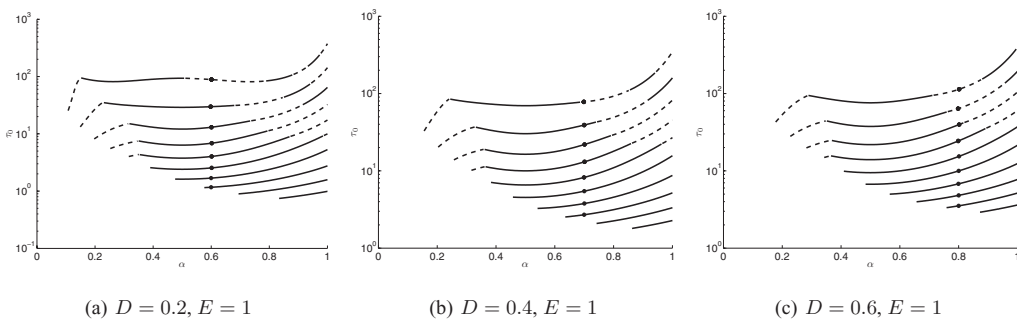
(a) $D = 0.2$, $E = 1$ (b) $D = 0.4$, $E = 1$ (c) $D = 0.6$, $E = 1$.

FIGURE 17. Plot of τ_0 versus α for various f with $E = 1$ and $D = 0.2$ (left), $D = 0.4$ (centre) and $D = 0.6$ (right). The extent of the curves in α increases in f, as does the value of τ_0 for any given α. For α where the curves are solid (dashed), the dominant instability is the synchronous (asynchronous) mode. The dot denotes the equilibrium location α_e; for curves without a dot, a dynamic competition instability is possible. The values of f are as follows: left figure: $f = 0.6181$, 0.6494, 0.6808, 0.7121, 0.7434, 0.7747, 0.8060, 0.8374, 0.8687, 0.9000; centre figure: $f = 0.6772$, 0.7019, 0.7267, 0.7514, 0.7762, 0.8010, 0.8257, 0.8505, 0.8752, 0.9000; right figure: $f = 0.6980$, 0.7204, 0.7429, 0.7653, 0.7878, 0.8102, 0.8327, 0.8551, 0.8776, 0.9000.

to asynchronous oscillations, can be the dominant instability depending on the value of α. In contrast, for the GM and GS models studied in [25], the synchronous mode was always the dominant instability. Using the numerical procedure used to produce the Hopf bifurcation curves of Section 2.4, we solve $g_j(i\lambda_I) = 0$ to obtain curves $\tau_{0j}(\alpha)$ and $\lambda_{Ij}^0(\alpha)$.

Treating α as the independent variable, we fix D and E and generate Hopf curves for values of f in the interval $f_c < f \leqslant 0.9$, where $\alpha_c = 1$ when $f = f_c$. In Figure 16, this corresponds to a vertical traversal from the dotted curve down towards the D/E-axis. Results are presented on a semi-log plot for three ratios of D/E. In Figures 17(a)–(c), we take $E = 1$ and $D = 0.2, 0.4$ and 0.6. Similar plots were made (not shown) for the same ratios of D/E but with $D = 1$ and $E = 5, 2.5, 1.67$, yielding qualitatively similar plots. For values of α where the curves are solid, the synchronous mode is the dominant instability ($\tau_0 \equiv \tau_{00}$), whereas for the portions of the curves where they are dashed, the asynchronous mode is dominant ($\tau_0 \equiv \tau_{01}$). The curves are ordered such that for a given α, $\tau_0(\alpha)$ increases with increasing f. We end the plot for $\alpha < \alpha_c$, that is, values of α for which the τ_{01} curve does not exist; the corresponding complex conjugate imaginary eigenvalues approach the origin as $\alpha \to \alpha_c^+$ the same way that $\lambda_{I1}^0 \to 0$ as $D \to D_{c2}^-$ as discussed in Section 2.4. The equilibrium location α_e is denoted by a dot; in the absence of a dot, the condition $\alpha_e < \alpha_c$ is satisfied and a dynamic competition instability is possible. In Figure 17(a), τ_{00} and τ_{01} are almost equal for α sufficiently near unity, and the breaks in the curves appear to be due to differences in decimal places beyond the precision of the solver.

For a given α, the quasi-equilibrium is stable (unstable) when τ is below (above) the curve. Thus, because the spike motion from (3.15) is directed monotonically towards the equilibrium location, dynamic oscillatory instabilities are only possible when either the slope of τ_0 is negative when $\alpha < \alpha_e$ or positive when $\alpha > \alpha_e$. From Figures 17(a)–(c), we see that for f near f_c, the only possibility for a dynamic oscillatory instability is when the initial spike locations satisfy $\alpha(0) > \alpha_e$ and τ satisfies $\tau_0(\alpha_e) < \tau < \tau_0(\alpha(0))$ (or
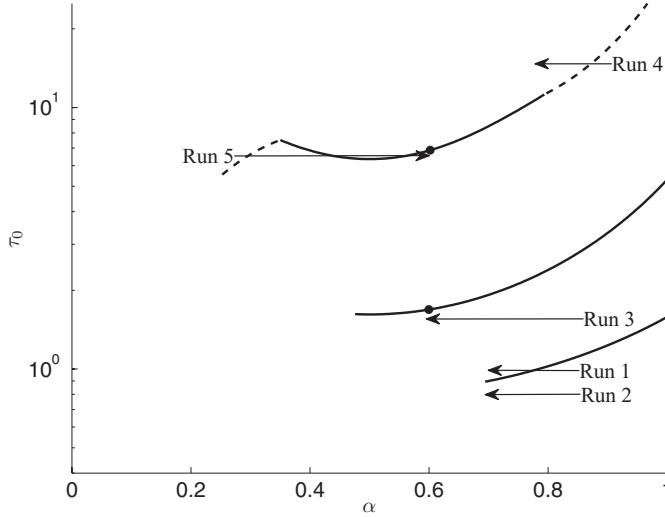
FIGURE 18. Hopf stability curves for (bottom to top) $f = 0.6494$, 0.7121 and 0.806. The arrows indicate the evolution of $\alpha(t)$, while the height of the arrows is only indicative of the value of τ used in the runs. Runs 1 and 2 are associated with the lowest curve, Run 3 with the middle curve and Runs 4 and 5 with the top curve. Solid curves indicate that $\tau_0 \equiv \tau_{00}$ (synchronous mode), while dashed curves indicate that $\tau_0 \equiv \tau_{01}$ (asynchronous mode). The curves are cut off on the left at $\alpha = \alpha_c$. The equilibrium point $\alpha_e = 0.6$ is indicated by a dot when the condition $\alpha_e > \alpha_c$ is satisfied.

$\tau_0(\alpha_c) < \tau < \tau_0(\alpha(0))$ if $\alpha_e < \alpha_c$), leading to the triggering of synchronous spike oscillations at some $t > 0$ as $\alpha \to \alpha_e^+$. For larger f, a similar scenario is possible for asynchronous oscillations. For still larger f, synchronous oscillations may be triggered when the initial spike location satisfies $\alpha(0) < \alpha_e$. This may occur after passage through a region of instability to asynchronous oscillations. In the next section, we illustrate these scenarios by solving numerically the full PDE system (1.5).

3.5 Numerical validation: symmetric quasi-equilibria

We now illustrate five different scenarios involving spike dynamics with parameters used to generate curves in Figure 17(a). For clarity, we reproduce the curves in Figure 18 on which we qualitatively annotate the dynamics of $\alpha(t)$ for each run. Below, we present the results of each run by plotting the spike amplitudes u_m and spike locations x_j versus time, produced by solving (1.5) with 4,000 grid points using MATLAB's pdepe() solver. In all runs, we took $\epsilon = 0.005$, $D = 0.2$ and $E = 1$, with f and τ being varied between the runs. The initial conditions are treated in the same way as described in Section 2.5, where the quasi-equilibrium solution in (3.4) is taken as the initial conditions, and a small value of τ is used to solve forward in time until a true quasi-equilibrium solution is reached. While the time required for the initiation process is small compared to ϵ^{-2}, the spikes still drift during this time. As such, appropriate compensations were made in the initial conditions so that the spike locations were in their desired locations at the end of the initiation. All values for the initial spike locations $\alpha(0)$ quoted below refer to their locations at the end of the initiation.

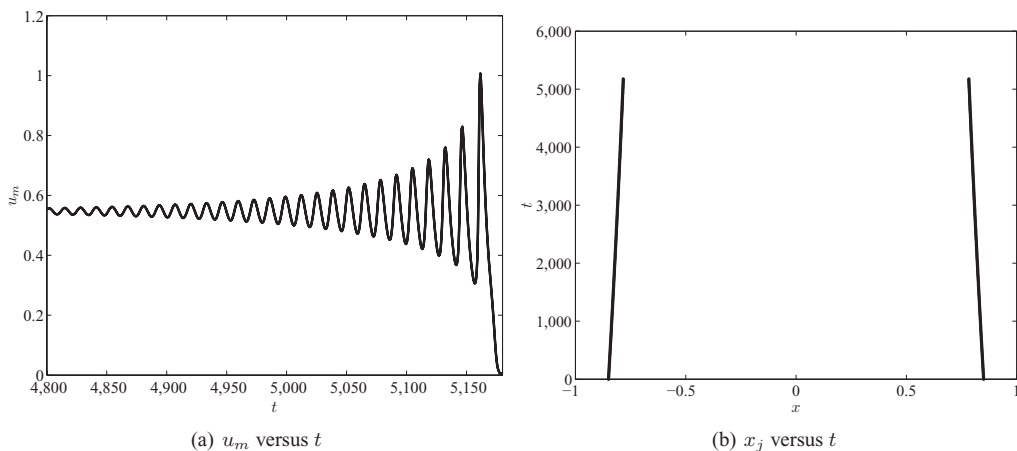(a) u_m versus t

(b) x_j versus t

FIGURE 19. Run 1: Dynamic synchronous oscillatory instability for $\epsilon = 0.005$, $D = 0.2$, $E = 1$, $f = 0.6494$, $\tau = 1.05$ and $\alpha(0) = 0.85$. In the left figure, synchronous oscillations of the spike amplitudes grow in time at the onset of instability and annihilate at some later time. In the right figure, we show a comparison between the evolution of the spike locations and the dynamics (3.15). They are indistinguishable in this plot.

In Run 1, we take $\alpha(0) = 0.85$, $f = 0.6494$ and $\tau = 1.05 < \tau_0(\alpha(0))$, so that the quasi-equilibrium is initially stable at $t = 0$. However, as indicated in Figure 18, our theory predicts that a dynamic synchronous oscillatory instability is triggered at some $t > 0$ when α decreases below the synchronous stability threshold indicated by the solid curve in this figure. That is, for some time $t > 0$, the condition $\tau > \tau_0(\alpha(t))$ is satisfied, at which time the solution becomes unstable to synchronous oscillations. In Figure 19(a) we show the amplitudes of the two spikes, which are indistinguishable, after the onset of the synchronous Hopf instability. The spikes annihilate before α reaches α_c, implying that the annihilation was not due to a competition instability. In Figure 19(b), we show a favourable comparison between the slow time evolution of the location of the spikes and the dynamics in (3.15) before the time of annihilation.

With the initial conditions and the other parameters unchanged, for Run 2 we decrease τ to $\tau = 0.8$ so that the Hopf stability threshold is not crossed at any point in the dynamics. However, because $\alpha_e < \alpha_c$, a competition instability occurs as $\alpha(t)$ decreases below α_c. This scenario is illustrated in Figure 18. In Figure 20(a), we show the annihilation of one of the spikes after the threshold $\alpha(t) < \alpha_c$ is crossed. In Figure 20(b), we show a favourable comparison between the numerical spike dynamics and that predicted by (3.15) up to the time of annihilation of the right spike. After the annihilation, the remaining spike evolves according to the one-spike dynamical result of [27].

In Run 3, we keep τ unchanged but increase f to $f = 0.7121$ so that $\alpha_c < \alpha_e$ and τ remains below $\tau_0(\alpha)$ for all values of α in the interval $(\alpha_e, \alpha(0))$. Thus, no dynamic instabilities occur, and the spikes evolve monotonically to their equilibrium locations at $\alpha_e = 0.6$. The motion of the spikes, along with the dynamics (3.15), are shown in Figure 20(c).

(a) u_m versus t, $\alpha_e < \alpha_c$ (b) x_j versus t, $\alpha_e < \alpha_c$ (c) x_j versus t, $\alpha_e > \alpha_c$
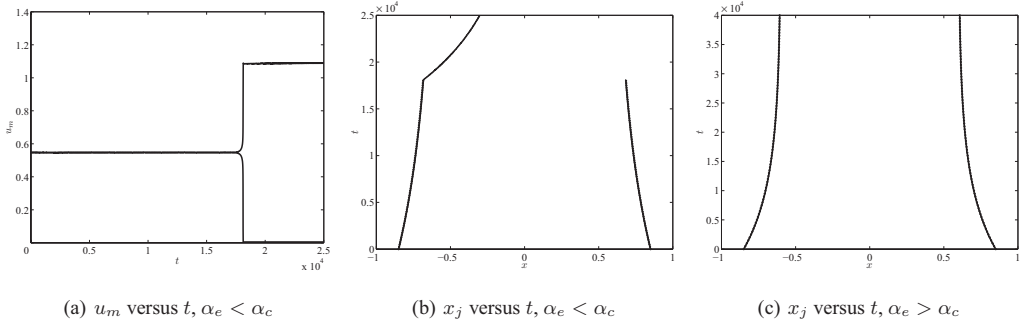
FIGURE 20. Runs 2 and 3: The left and centre figures (Run 2) are plots of the spike amplitudes and locations versus time in the case of a dynamic competition instability for $\epsilon = 0.005$, $D = 0.2$, $E = 1$, $f = 0.6494$, $\tau = 0.8$ and $\alpha(0) = 0.85$. In the right figure (Run 3), f is increased to $f = 0.7172$ so that no instabilities are triggered and the spikes approach the equilibrium location $\alpha_e = 0.6$.

In Run 4, we take $\alpha(0) = 0.91$, $f = 0.806$ and $\tau = 15 < \tau_0(\alpha(0))$. This run is similar to Run 1 except that a dynamic asynchronous instability is triggered instead of a synchronous instability. This scenario is shown in Figure 18; for some $t > 0$, $\alpha(t)$ will satisfy $\tau > \tau_0(\alpha(t))$, initiating an asynchronous instability. In Figure 21(a) we show asynchronous spike amplitude oscillations resulting from the triggering of an asynchronous Hopf instability. As in Run 1, the spikes annihilate at some time after onset but before α has reached α_c, implying that the annihilation was not due to a competition instability. In Figure 21(b), we show a favourable comparison between the slow spike dynamics before the annihilation event and the one predicted by (3.15). For this run, we perturbed the initial condition as in (2.63), where $d_0 = 1$ and $d_1 = -1$ in accordance with the eigenvector associated with the asynchronous mode. While the perturbation initially decayed and appeared to be unnoticeable by the time the spikes approached the asynchronous instability threshold, enough of the initial perturbation remained to trigger the asynchronous instability. Without the initial perturbation, a synchronous instability developed due to the nearby synchronous instability threshold (not shown in Figure 18).

In Run 5, we keep the parameters as in Run 4, except we set $\alpha(0) = 0.28$ and $\tau = 6.6$, so that $\tau > \tau_0(\alpha(0)) = \tau_{01}$. Thus, the solution starts above the asynchronous stability threshold but gains stability as $\alpha(t)$ increases towards α_e. However, before reaching α_e, a loss of stability to synchronous oscillations occurs before stability is regained after $\alpha(t)$ drifts across the zone of synchronous instability. The evolution through the zones of stability and instability is depicted in Figure 18. In Figures 22(a) and (b), we show the spike amplitudes and locations versus time for the entire duration of dynamics. Note that the spikes evolve according to (3.15) even when $\alpha(t)$ is in an unstable region. Figure 22(a) shows the triggering of two distinct types of instabilities, each of which are eventually extinguished as time increases. The first of these instabilities, as previously mentioned, is to the asynchronous mode and is magnified in Figure 22(c). The initial conditions were perturbed in the same way as in Run 4. After an initial growth in the amplitude of asynchronous oscillations, the spike amplitudes approach their quasi-equilibrium value as they move into the zone of stability. At a later time, shown in Figure 22(d), the spikes move into a zone of synchronous instability where the amplitude
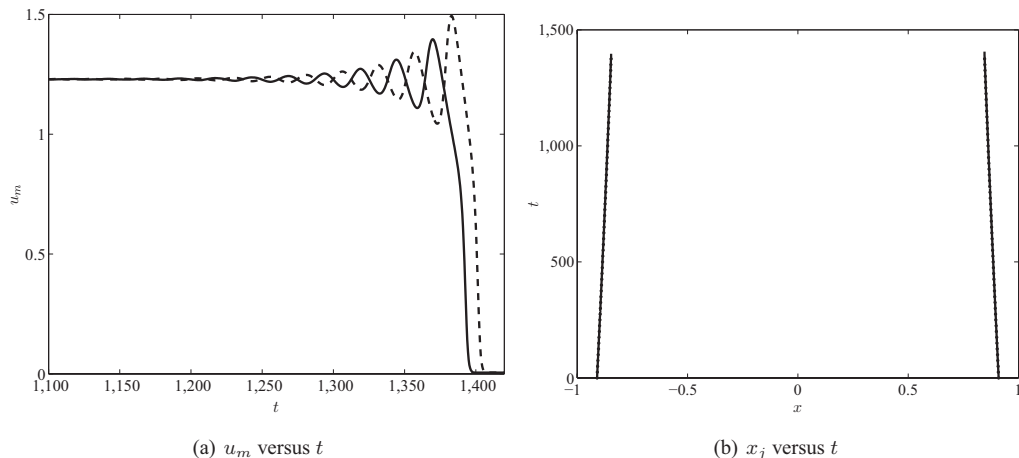
(a) u_m versus t (b) x_j versus t

FIGURE 21. Run 4: Dynamic asynchronous oscillatory instability for $\epsilon = 0.005$, $D = 0.2$, $E = 1$, $f = 0.806$, $\tau = 15$ and $\alpha(0) = 0.91$. In the left figure, asynchronous oscillations of the left (solid) and right (dashed) spike amplitudes grow in time at the onset of instability and annihilate at some later time. In the right figure, we show a comparison between the evolution of the spike locations and the dynamics (3.15) up to the time of annihilation.

of synchronous oscillations grow. These oscillations decay as the spikes move out of the unstable region and towards their equilibrium locations. Note that the frequency of synchronous oscillations is approximately four times that of the asynchronous oscillations, which is consistent with our calculations (not shown). In other experiments, it was observed that starting too far above the asynchronous stability curve led to an annihilation of one of the spikes. Further, the movement of the spikes through a zone of instability without annihilating may be facilitated by ϵ sufficiently large; for small ϵ where the time spent in unstable regions is significantly longer, annihilation events may occur.

Finally, we note that all of these experiments involve only $\mathcal{O}(1)$ instabilities. For numerical computations involving instabilities to $\mathcal{O}(\epsilon^2)$ eigenvalues, see [27].

4 Discussion

We have analysed the stability of localized spike patterns for two closely related singularly perturbed RD systems with Brusselator kinetics. The derivation of the NLEP for the Brusselator is more intricate than in previous stability analyses of spike patterns for the GM and GS models [12,30,32] owing to the non-trivial background state for the activator and the existence of two non-local terms arising from the $\mathcal{O}(\epsilon^{-1})$ coefficient in (1.3b) and (1.5b). A combination of rigorous and numerical analysis was used to obtain stability thresholds from this NLEP, and the results have been confirmed with full numerical simulations of the PDE systems. For (1.5), an NLEP stability theory is applied to a quasi-steady, two-spike evolution, and our results show the existence of dynamically triggered instabilities depending on the parameter regime.

For both Brusselator models (1.5) and (1.3), our NLEP stability results show that as τ increases above a threshold, a Hopf bifurcation triggers either a synchronous or an

(a) u_m versus t

(b) x_j versus t

(c) u_m versus t, first instability: asynchronous

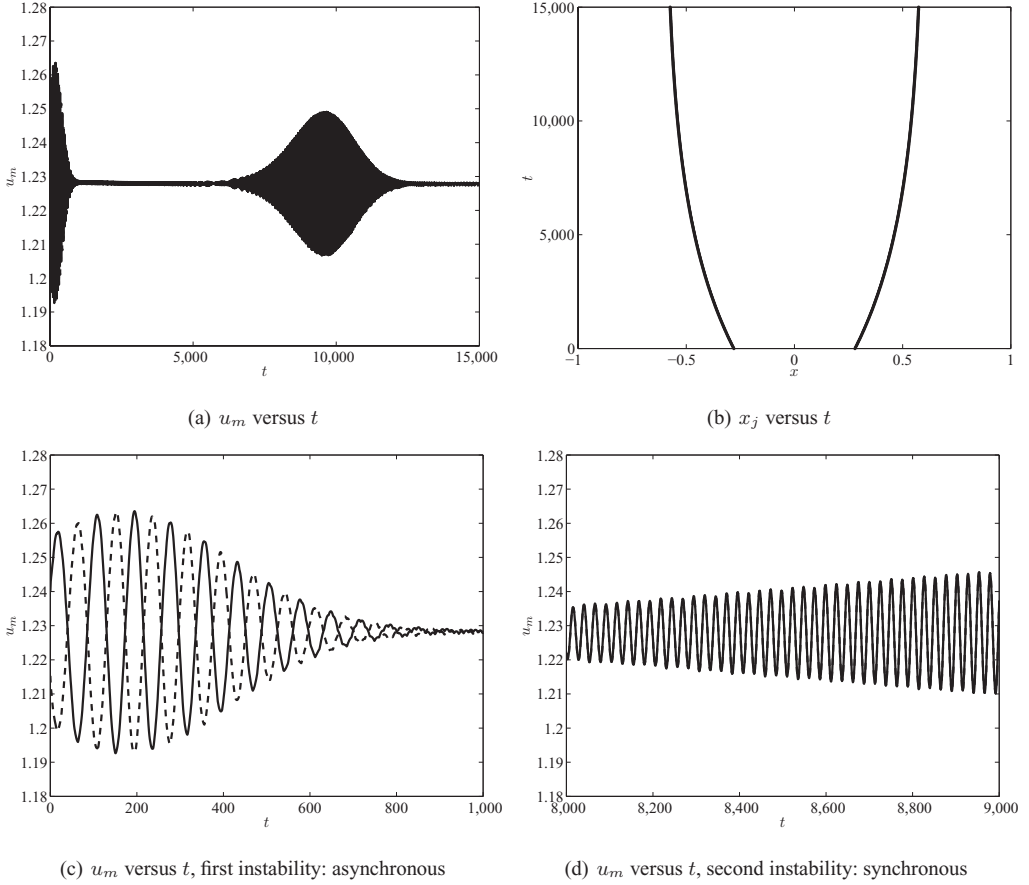(d) u_m versus t, second instability: synchronous

FIGURE 22. Run 5: Synchronous and asynchronous instabilities for $\epsilon = 0.005$, $D = 0.2$, $E = 1$, $f = 0.806$, $\tau = 6.6$ and $\alpha(0) = 0.28$. The top left figure shows the spike amplitudes as the spikes move through zones of stability and instability and eventually to their equilibrium locations (top right). The first instability is to the asynchronous mode (bottom left) and the second instability is to the synchronous mode (bottom right). In the bottom left figure, the solid (dashed) curve is the amplitude of the left (right) spike. In the bottom right figure, the spike amplitudes are indistinguishable.

asynchronous oscillation in the spike amplitudes. The nature of the oscillation depends on the parameter values of f and D, and for (1.5), also on the inter-spike distance. Our full numerical simulations of the PDE systems confirm the two modes of oscillation. Furthermore, our numerical results suggest that the synchronous instability, which leads to the annihilation of spikes, is subcritical, while the asynchronous instability is supercritical. The existence of robust asynchronous spike amplitude oscillations observed in our analysis of the Brusselator model has not been reported in NLEP stability studies of other RD systems (cf. [12, 32]).

A key open problem, suggested by our results, is to perform a weakly nonlinear theory on the Brusselator model, and on related RD systems with spike solutions, to analyse whether spike amplitude oscillations are subcritical or supercritical.
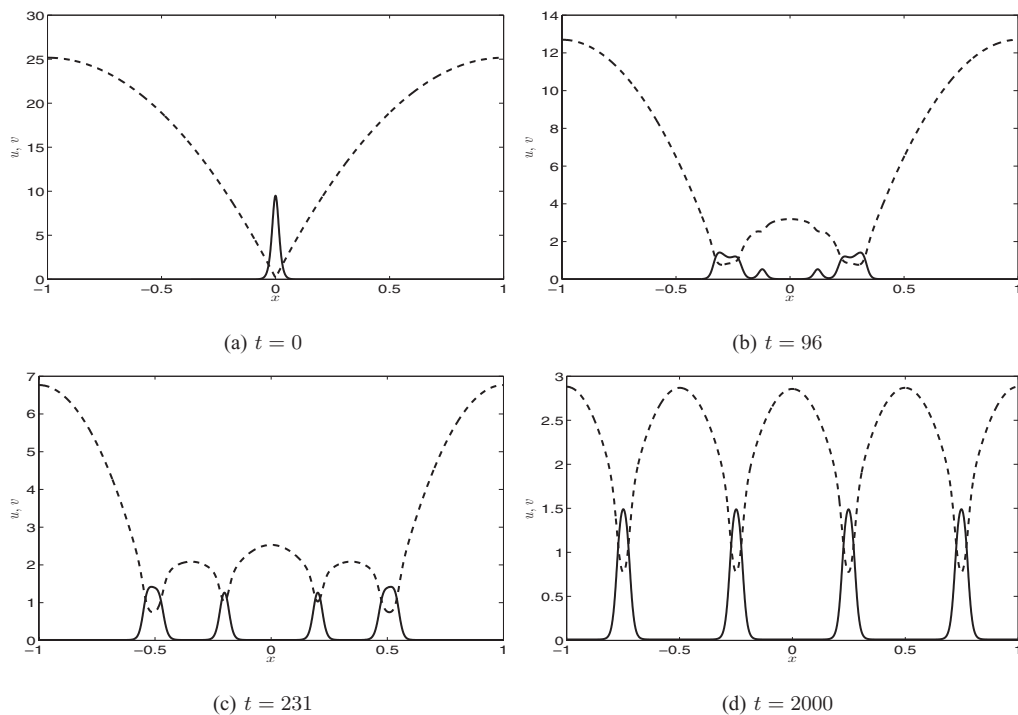
FIGURE 23. Self-replication of a pulse for (1.3) with $\epsilon = 0.01$, $A = 0$, $D = 0.02$, $f = 0.95$ and $\tau = 0.001$. The solid curve is u, while the dotted curve is v.

Another interesting open problem is to try to extend the pulse-splitting analysis of [4, 13, 16] to analyse a similar pulse-splitting phenomena for the Brusselator model (1.3) that occurs in the regime when f approaches unity. Starting from a one-pulse quasi-equilibrium state, in Figure 23 we show numerical results computed from (1.3) for the parameter set $\epsilon = 0.01$, $A = 0$, $D = 0.02$, $f = 0.95$ and $\tau = 0.001$. Such a pulse-splitting behaviour has not been reported previously for the Brusselator model.

A final open problem is to analyse (1.3) in a two-dimensional spatial domain, where localized spot patterns undergo either self-replication, competition or oscillatory instabilities depending on the parameter regime. The determination of phase diagrams in parameter space for these instabilities is critical for characterizing dynamic bifurcations of localized spot patterns.

Acknowledgements

Appendix A Scaling analysis of the Brusselator model

In this appendix we outline the scaling analysis of [27] for the existence of spikes to (1.2). For $\epsilon_0 \to 0$, U has an inner scale U_{inn} near a spike and an outer scale U_{out} away from

a spike. In contrast, V has only one scale across the interval, which is induced by the boundary feed so that $V = \mathcal{O}(\mathscr{A}_0)$. In order to obtain a homoclinic solution characterizing the spike profile, we require in the inner region near a spike that $U_{\text{inn}}^2 V \sim U_{\text{inn}}$. Therefore, $U_{\text{inn}} = \mathcal{O}\left(\mathscr{A}_0^{-1}\right)$.

Next, since U is localized, we require from (1.2b) that $DV_{xx} \sim \int_{-1}^{1} VU^2 \, dx$. Since the integrand has an $\mathcal{O}(\epsilon_0)$ support near a spike, this yields that $\mathscr{A}_0 \sim \epsilon_0/\mathscr{A}_0$, which implies that $\mathscr{A}_0 = \mathcal{O}(\epsilon_0^{1/2})$. Consequently, we conclude that $U_{\text{inn}} = \mathcal{O}(\epsilon_0^{-1/2})$ and $V_{\text{inn}} = \mathcal{O}(\epsilon_0^{1/2})$. Finally, from (1.2b) we must balance the scales of DV_{xx} and BU across $-1 < x < 1$, which yields that $U_{\text{out}} = \mathcal{O}(\epsilon_0^{1/2})$, and consequently $\mathscr{E}_0 = \mathcal{O}(\epsilon_0^{1/2})$ from (1.2a).

Therefore, we will consider (1.2) in the parameter regime where $\mathscr{A}_0 = \epsilon_0^{1/2} A_0$ and $\mathscr{E}_0 = \epsilon_0^{1/2} E_0$ for some non-negative $\mathcal{O}(1)$ constants A_0 and E_0. We also give an alternate scaling for the $A_0 = 0$ case.

Firstly, we introduce the rescaled $\mathcal{O}(1)$ variables u and v and the new temporal variable σ, defined by

$$U = \epsilon_0^{-1/2} u_c u, \quad V = \epsilon_0^{1/2} v_c v, \quad t = T\sigma.$$

From (1.2), we then obtain the system

$$\frac{1}{T(B_0+1)} u_\sigma = \left(\frac{\epsilon_0}{\sqrt{B_0+1}}\right)^2 u_{xx} + \frac{\epsilon_0 E_0}{u_c(B_0+1)} - u + \frac{u_c v_c}{B_0+1} vu^2, \quad \text{(A.1a)}$$

$$\frac{\sqrt{B_0+1}}{u_c^2 T} v_\sigma = \frac{D_0\sqrt{B_0+1}}{u_c^2} v_{xx} + \frac{\sqrt{B_0+1}}{\epsilon_0}\left(\frac{B_0}{u_c v_c} u - vu^2\right). \quad \text{(A.1b)}$$

Choosing $T = 1/(B_0+1)$ and $u_c v_c = B_0$ in (A.1), and defining the new parameters ϵ, D, E, f and τ as

$$\epsilon \equiv \frac{\epsilon_0}{\sqrt{B_0+1}}, \quad D \equiv \frac{D_0\sqrt{B_0+1}}{u_c^2}, \quad E \equiv \frac{E_0}{u_c\sqrt{B_0+1}}, \quad f \equiv \frac{B_0}{B_0+1},$$

$$\tau \equiv \frac{(B_0+1)^{3/2}}{u_c^2}, \quad \text{(A.2)}$$

we obtain the system

$$u_\sigma = \epsilon^2 u_{xx} + \epsilon E - u + fvu^2, \quad -1 < x < 1, \quad u_x(\pm 1, \sigma) = 0, \quad \text{(A.3a)}$$

$$\tau v_\sigma = Dv_{xx} + \frac{1}{\epsilon}\left(u - vu^2\right), \quad -1 < x < 1, \quad v_x(\pm 1, \sigma) = \pm A_0/v_c, \quad \text{(A.3b)}$$

valid for $A_0 \geqslant 0$. If $A_0 > 0$, we choose $v_c = A_0$ so that $u_c = B_0/A_0$. Replacing the time variable σ with t in (A.3), the Brusselator model with asymptotically small boundary feed of the inhibitor is written in the form (1.5) where σ is replaced by t, and ϵ, f, E, D and τ are defined in terms of the original variables by (1.6).

Alternatively, if $A_0 = 0$, we may choose $u_c = E_0/\sqrt{B_0+1}$, so that $v_c = B_0\sqrt{B_0+1}/E_0$, resulting in the parameter E in (A.2) and (A.3) being unity. In this case the Brusselator model with no flux boundary conditions is (1.3), where ϵ, f, D and τ are as defined in (1.4).

References

[1] CHEN, W. & WARD, M. J. (1999) Oscillatory instabilities and dynamics of multi-spike patterns for the one-dimensional Gray-Scott model. *Europ. J. Appl. Math.* **20**(2), 187–214.

[2] DOELMAN, A., ECKHAUS, W. & KAPER, T. J. (2000) Slowly-modulated two-pulse solutions in the Gray-Scott model I: Asymptotic construction and stability. *SIAM J. Appl. Math.* **61**(3), 1080–1102.

[3] DOELMAN, A., ECKHAUS, W. & KAPER, T. J. (2001) Slowly modulated two-pulse solutions in the Gray-Scott model II: Geometric theory, bifurcations, and splitting dynamics. *SIAM J. Appl. Math.* **66**(6), 2036–2062.

[4] DOELMAN, A., GARDNER, R. A. & KAPER, T. J. (1998) Stability analysis of singular patterns in the 1D Gray-Scott model: A matched asymptotic approach. *Physica D* **122**, 1–36.

[5] DOELMAN, A., GARDNER, R. A. & KAPER, T. J. (2001) Large stable pulse solutions in reaction-diffusion equations. *Indiana Univ. Math. J.* **50**(1), 443–507.

[6] DOELMAN, A. & KAPER, T. (2003) Semistrong pulse interactions in a class of coupled reaction-diffusion equations. *SIAM J. Appl. Dyn. Sys.* **2**(1), 53–96.

[7] DOELMAN, A., KAPER, T. J. & PROMISLOW, K. (2007) Nonlinear asymptotic stability of the semistrong pulse dynamics in a regularized Gierer-Meinhardt model. *SIAM J. Math. Anal.* **38**(6), 1760–1787.

[8] IRON, D. & WARD, M. J. (2002) The dynamics of multi-spike solutions for the one-dimensional Gierer-Meinhardt model. *SIAM J. Appl. Math.* **62**(6), 1924–1951.

[9] IRON, D., WARD, M. J. & WEI, J. (2001) The stability of spike solutions to the one-dimensional Gierer-Meinhardt model. *Physica D* **150**(1–2), 25–62.

[10] IRON, D., WEI, J. & WINTER, M. (2004) Stability analysis of turing patterns generated by the Schnakenberg model. *J. Math. Biol.* **49**(4), 358–390.

[11] KERNER, B. S. & OSIPOV, V. V. (1994) *Autosolitons: A New Approach to Problem of Self-Organization and Turbulence*, Kluwer, Dordrecht, Netherlands.

[12] KOLOKOLNIKOV, T., WARD, M. J. & WEI, J. (2005) The existence and stability of spike equilibria in the one-dimensional Gray-Scott model: The low feed rate regime. *Stud. Appl. Math.* **115**(1), 21–71.

[13] KOLOKOLNIKOV, T., WARD, M. J. & WEI, J. (2005) The existence and stability of spike equilibria in the one-dimensional Gray-Scott model: The pulse-splitting regime. *Physica D* **202**(3–4), 258–293.

[14] KOLOKOLNIKOV, T., WARD, M. J. & WEI, J. (accepted) The stability of steady-state hot-spot patterns for a reaction-diffusion model of urban crime. *DCDS-B* 34.

[15] LIN, C. S., NI, W. M. & TAKAGI, I. (1988) Large amplitude stationary solutions to a chemotaxis system. *J. Diff. Equ.* **72**, 1–27.

[16] MURATOV, C. B. & OSIPOV, V. V. (2000) Static spike autosolitons in the Gray-Scott model. *J. Phys. A: Math. Gen.* **33**, 8893–8916.

[17] MURATOV, C. B. & OSIPOV, V. V. (2002) Stability of the static spike autosolitons in the Gray–Scott model. *SIAM J. Appl. Math.* **62**(5), 1463–1487.

[18] NICOLIS, G. & PRIGOGINE, I. (1977) *Self-Organization in Nonequilibrium Systems*, Wiley, New York.

[19] NISHIURA, Y. (2002) *Far-From Equilibrium Dynamics, Translations of Mathematical Monographs*, Vol. 209, AMS, , Providence, RI.

[20] PENA, B. & PEREZ-GARCIA, C. (2001) Stability of turing patterns in the Brusselator model. *Phys. Rev. E.* **64**, 056213

[21] PENG, R. & WANG, M. (2005) Pattern formation in the Brusselator system. *J. Math. Anal. Appl.* **309**(1), 151–166.

[22] PENG, R. & YANG, M. (2009) On steady-state solutions of the Brusselator-type system. *Nonlinear Anal. Theory, Methods Appl.* **71**(3–4), 1389–1394.

[23] SCHENK, C. P., OR-GUIL, M., BODE, M. & PURWINS, H. (1997) Interacting pulses in three-component reaction-diffusion systems on two-dimensional domains. *Phys. Rev. Lett.* **78**(19), 3781–3784.

[24] SHORT, M. B., BERTOZZI, A. L. & BRANTINGHAM, P. J. (2010) Nonlinear patterns in urban crime – Hotpsots, bifurcations, and suppression. *SIAM J. Appl. Dyn. Sys.* **9**(2), 462–483.

[25] SUN, W., WARD, M. J. & RUSSELL, R. (2005) The slow dynamics of two-spike solutions for the Gray-Scott and Gierer-Meinhardt systems: Competition and oscillatory instabilities. *SIAM J. Appl. Dyn. Sys.* **4**(4), 904–953.

[26] TZOU, J. C., BAYLISS, A., MATKOWSKY, B. J. & VOLPERT, V. A. (2011) Interaction of turing and Hopf modes in the superdiffusive brusselator model near a co-dimension two bifurcation point. *Math. Model. Nat. Phenom.* **6**(1), 87–118.

[27] TZOU, J. C., BAYLISS, A., MATKOWSKY, B. J. & VOLPERT, V. A. (2011) Stationary and slowly moving localized pulses in a singularly perturbed Brusselator model. *Eur. J. Appl. Math.* **22**(5), 423–453.

[28] VANAG, V. K. (2004) Waves and patterns in reaction diffusion systems. Belousov-Zhabotinsky reaction in water-in oil microemulsions. *Phys. Usp.* **47**, 923–941.

[29] VANAG, V. K. & EPSTEIN, I. R. (2007) Localized patterns in reaction-diffusion systems. *Chaos* **17**(3), 037110.

[30] VAN DER PLOEG, H. & DOELMAN, A. (2005) Stability of spatially periodic pulse patterns in a class of singularly perturbed reaction-diffusion equations. *Indiana Univ. Math. J.* **54**(5), 1219–1301.

[31] WARD, M. J. & WEI, J. (2002) The existence and stability of asymmetric spike patterns for the Schnakenberg model. *Stud. Appl. Math.* **109**(3), 229–264.

[32] WARD, M. J. & WEI, J. (2003) Hopf bifurcations and oscillatory instabilities of spike solutions for the one-dimensional Gierer-Meinhardt model. *J. Nonlinear Sci.* **13**(2), 209–264.

[33] WARD, M. J. & WEI, J., (2003) Hopf bifurcation of spike solutions for the shadow Gierer-Meinhardt model. *Europ. J. Appl. Math.* **14**(6), 677–711.

[34] WEI, J. (1999) On single interior spike solutions for the Gierer-Meinhardt system: Uniqueness and spectrum estimates. *Eur. J. Appl. Math.* **10**(4), 353–378.

[35] WEI, J. (2008) Existence and stability of spikes for the Gierer-Meinhardt system. In: M. Chipot (editor), *Handbook of Differential Equations, Stationary Partial Differential Equations*, Vol. 5, Elsevier, Waltham, MA, pp. 489–581.

[36] WITTENBERG, R. & HOLMES, P. (1997) The limited effectiveness of normal forms: A critical review and extension of local bifurcation studies of the Brusselator PDE. *Physica D* **100**, 1–40.